

# Materials Advances

Accepted Manuscript

This article can be cited before page numbers have been issued, to do this please use: Md. R. Hossain, S. Khanom, A. K. Paul, P. Mondal and F. Ahmed, *Mater. Adv.*, 2026, DOI: 10.1039/D6MA00290K.



This is an Accepted Manuscript, which has been through the Royal Society of Chemistry peer review process and has been accepted for publication.

Accepted Manuscripts are published online shortly after acceptance, before technical editing, formatting and proof reading. Using this free service, authors can make their results available to the community, in citable form, before we publish the edited article. We will replace this Accepted Manuscript with the edited and formatted Advance Article as soon as it is available.

You can find more information about Accepted Manuscripts in the [Information for Authors](#).

Please note that technical editing may introduce minor changes to the text and/or graphics, which may alter content. The journal's standard [Terms & Conditions](#) and the [Ethical guidelines](#) still apply. In no event shall the Royal Society of Chemistry be held responsible for any errors or omissions in this Accepted Manuscript or any consequences arising from the use of any information it contains.

## Data Availability Statement

The data supporting the findings of this study, including structural parameters, magnetic moments, elastic, electronic band structures, of  $A_3CrO_4$  ( $A = Mg, Ca, Sr$ ) alkali-metal oxides are available from the corresponding author upon reasonable request. No restrictions apply to data sharing.



# Evaluation of Pressure Induced Physical and Magnetic Properties of $A_3CrO_4$ (A=Mg, Ca, Sr) Alkali-Metal Oxides for Spintronics Applications Via DFT

Md. Rony Hossain<sup>a,b,\*</sup>, Mst. Shamima Khanom<sup>b</sup>, Prianka Mondal<sup>c</sup>, Akash Kumer Paul<sup>b</sup>, Farid Ahmed<sup>b</sup>

<sup>a</sup>Department of Software Engineering, Daffodil International University, DSC, Birulia, Savar, Dhaka-1216, Bangladesh

<sup>b</sup>Department of Physics, Jahangirnagar University, Savar, Dhaka, 1342, Bangladesh

<sup>c</sup>Dhaka University of Engineering & Technology, Gazipur, 1707, Bangladesh

Corresponding Author Email: rony.hossainb@gmail.com

## Abstract

The present study employs density functional theory (DFT) within the CASTEP framework to systematically investigate the pressure-tunable structural, electronic and magnetic properties of  $A_3CrO_4$  (A = Mg, Ca, Sr) alkali-metal oxides using GGA-PBE, GGA+U and GGA-PBEsol functionals. Structural optimization confirms that all  $A_3CrO_4$  (A = Mg, Ca, Sr) compounds crystallize in the cubic  $P\bar{m}3m$  space group, with ferromagnetic (FM) ordering consistently more stable than non-magnetic (NM) states across the entire pressure range of 0–30 GPa.  $Mg_3CrO_4$  and  $Ca_3CrO_4$  exhibit robust FM ground states with total magnetic moments of +4.0 to  $-4.1 \mu_B$  maintaining half-metallicity under hydrostatic pressures up to 30 GPa. In contrast,  $Sr_3CrO_4$  undergoes a pressure-induced magnetic phase transition, with its magnetic moment reversing sign at 20–30 GPa, indicating a shift toward antiferromagnetic (AFM) or ferrimagnetic ordering. Elastic constant analysis confirms dynamic stability across the entire pressure range (0–30 GPa). While  $Mg_3CrO_4$  remains brittle under compression,  $Ca_3CrO_4$  and  $Sr_3CrO_4$  exhibit pressure-induced ductility transitions, transforming from brittle to ductile behavior at higher pressures. Electronic structure calculations reveal persistent half-metallicity, with spin-down channels retaining wide band gaps and spin-up channels displaying metallic behavior. The application of Hubbard corrections (GGA+U) further validates the robustness of the electronic properties. The average sound velocity, Debye temperature, Debye frequency, melting temperature and Gruneisen parameter were analyzed under pressures up to 30 GPa.  $Mg_3CrO_4$  and  $Ca_3CrO_4$  show a steady increase in sound velocity, Debye temperature, and frequency, indicating lattice stiffening, stronger bonding and enhanced thermal stability. In contrast,  $Sr_3CrO_4$  exhibits anomalous behavior, with values rising up to 20 GPa but slightly decreasing at 30 GPa, consistent with its pressure-induced magnetic reversal. Melting temperatures increase significantly for all



compounds, confirming their suitability for high-temperature and high-pressure applications. The interplay between pressure and functional analyzing in these Cr-based compounds provides valuable insights for advancing spintronics and functional materials design.

**Keywords:** Density functional theory; Half-metallicity; Electronic band structure; Magnetic properties; High-pressure effects; Mechanical properties; Spintronics.

## 1. Introduction

Spintronics an emerging field utilizes the electron's intrinsic spin in addition to its charge to store, process, and transmit information, offering potential for faster, smaller, and more energy-efficient devices compared to conventional electronics<sup>1-3</sup>. This discipline is fundamentally driven by materials exhibiting high spin polarization, prolonged spin coherence times, and robust half-metallicity, particularly at room temperature<sup>2,4</sup>. Half-metallic ferromagnets (HMFs) are particularly attractive due to their unique electronic structure, where one spin channel is metallic while the other is semiconducting, leading to 100% spin polarization at the Fermi level<sup>5</sup>. This property makes half-metals ideal candidates for generating fully spin-polarized currents, which are essential for high-efficiency spintronic devices such as magnetic tunnel junctions (MTJs), spin valves, and spin-based transistors. A recent study proposed single-molecule optoelectronic devices using half-metallic FeN<sub>4</sub>-doped armchair graphene nanoribbons as electrodes coupled with metalloporphyrin molecules, achieving excellent spin-filtering effects through photo galvanic mechanisms<sup>6</sup>. The surface stability of half-metallicity is critical for device performance, as demonstrated in CrYCoAl, where surface effects were analyzed to ensure high spin polarization in thin-film configurations essential for MTJs<sup>7</sup>. Furthermore, 2D half-metallic systems such as MnAsS<sub>4</sub> and MnXSe<sub>4</sub> (X = As, Sb) exhibit intrinsic ferromagnetism with large spin gaps (up to 1.46 eV) and high Curie temperatures, addressing the long-standing challenge of thermal stability in nanoscale spintronic devices<sup>8</sup>. This characteristic makes half-metallic compounds highly promising for advanced spintronic and quantum information technologies such as spintronic applications<sup>9</sup>, including magnetic tunnel junctions<sup>10</sup>, spin injection systems<sup>11</sup>, magnetic data storage devices<sup>12</sup> and nonvolatile magnetic random-access memory technologies<sup>13</sup>.

Since the advent of spintronics in the early 1980s<sup>14</sup>, half-metallic ferromagnetic (HMF) materials have garnered significant attention in both theoretical and experimental domains of



materials science. The half-metallic nature was initially identified by de Groot and collaborators in semi-Heusler alloys such as NiMnSb and PtMnSb, marking a foundational advancement in spin-dependent electronic materials<sup>14</sup>. Subsequent computational and experimental investigations have identified half-metallic behavior in a wide range of compounds beyond the initial semi-Heusler systems. Notable examples include rutile-type TiO<sub>2</sub><sup>15</sup>, spinel FeCr<sub>2</sub>O<sub>4</sub><sup>16</sup>, full Heusler Ti<sub>2</sub>CoSi<sup>17</sup>, quadruple oxide perovskite CaCu<sub>3</sub>Fe<sub>2</sub>Re<sub>2</sub>O<sub>12</sub><sup>18</sup>, double perovskites La<sub>2</sub>CrNiO<sub>6</sub><sup>19</sup>, Sr<sub>2</sub>MnTaO<sub>6</sub><sup>20</sup>, Ba<sub>2</sub>YbTaO<sub>6</sub><sup>21</sup>, multiferroics RuC<sub>12</sub>/Al<sub>2</sub>S<sub>3</sub><sup>22</sup>, RuBrF/Sc<sub>2</sub>CO<sub>2</sub><sup>23</sup> zintl compounds EuMg<sub>2</sub>X<sub>2</sub> (X=Sb and Bi)<sup>24</sup> and XCr<sub>2</sub>Bi<sub>2</sub> (X=Ca, Sr)<sup>25</sup>. Benjamin Balke et al.<sup>26</sup> conducted a comprehensive study on the C1b compound CoTi<sub>1-x</sub>M<sub>x</sub>Sb (M = Fe, Mn, Cr, V) combining experimental techniques with first-principles calculations to demonstrate that selective substitution with 3d transition metals induces tunable half-metallic ferromagnetism, maintains crystalline stability, and achieves high Curie temperatures (>700K) thereby highlighting the material's potential for spintronic applications. Seungho Seong et al. employed XMCD and XAS to investigate temperature-dependent mixed-valent states of Cr ions in CrO<sub>2</sub> nanorods, providing direct experimental evidence of its half-metallic ferromagnetism<sup>27</sup>. Recently, Samira Barouni et al. synthesized a nanoscale semiconductive perovskite, La<sub>0.25</sub>Sr<sub>0.75</sub>Sn<sub>0.4</sub>In<sub>0.25</sub>Ru<sub>0.35</sub>O<sub>3</sub> (LSSIRuO), via co-doping of SrSnO<sub>3</sub>, demonstrating a narrowed band gap of 1.3 eV, robust conductivity, and low-temperature ferromagnetic ordering-highlighting its potential for optoelectronic, memory, and spintronic applications<sup>28</sup>. Rasik Ahmad Parray et al. investigated nanocrystalline Cr<sub>2</sub>NiAl inverse Heusler alloy synthesized via mechanical alloying, revealing a face-centered cubic X<sub>A</sub>/X<sub>α</sub> structure, aggregated morphology, tunable electronic behavior, room-temperature soft ferromagnetism, and improved magnetic properties with higher annealing temperatures<sup>29</sup>.

Transition metal oxides, especially those with perovskite or related structures, have garnered significant attention due to their tunable electronic and magnetic properties<sup>30-32</sup>. Chromium dioxide (CrO<sub>2</sub>), a well-known half-metallic ferromagnet, is a promising candidate for such applications due to its high Curie temperature and full spin polarization, though surface degradation remains a challenge<sup>33</sup>. Similarly, other chromium-based compounds such as ZnCrO<sub>3</sub> perovskites and Cr<sub>2</sub>O<sub>3</sub> have been studied for their half-metallic ferromagnetism and spintronic applications<sup>31,34</sup>. The precise engineering of these properties is crucial for advancing spintronic devices<sup>35</sup>. Mohammed El Amine Monir et al.<sup>36</sup> investigated X<sub>3</sub>FeO<sub>4</sub> (X = Mg, Ca, Sr) using DFT,



revealing ferromagnetic stability, semi-metallic behavior, and half-metallicity supported by elastic, electronic, and magnetic analyses. Their study also reported thermal parameters such as expansion coefficient, heat capacity, and Debye temperature, confirming the compounds' potential for advanced applications.

The objective of this study is to demonstrate the half-metallic nature of alkaline-earth chromates  $X_3CrO_4$  ( $X = Mg, Ca, Sr$ ) by analyzing their structural, electronic, and magnetic properties using DFT within the CASTEP framework under hydrostatic pressures ranging from 0–30 GPa. A central motivation is to investigate how the half-metallic gap evolves with applied pressure in  $Mg_3CrO_4$ ,  $Ca_3CrO_4$ , and  $Sr_3CrO_4$  employing GGA-PBE, GGA-PBEsol and GGA+U functionals. Understanding how variations in the alkaline-earth cation at the A-site influence these properties under pressure is key to designing new materials with enhanced performance for opto-spintronic applications. The paper is organized as follows: **Computational Details**: outlines the methodology, **Results and Discussion**: presents and interprets the structural, elastic, electronic, and magnetic findings and **Conclusions**: summarizes the main outcomes.

## 2. Computational Details

The DFT-based CASTEP computer software with the generalized gradient approximation (GGA) has been used for first-principles calculations. The Perdew-Burke-Ernzerhof (PBE) exchange-correlation functional with projected augmented-wave (PAW) pseudopotentials was selected for this calculation<sup>37–39</sup>. In the calculation of lattice optimization, the convergence parameters were set as follows: (i) the maximum ionic displacement 0.002 Å, (ii) the maximum stress component 0.10 GPa, (iii) 0.05 eV/Å is set for the maximum ionic force. The electromagnetic wave function extension in a plane-wave basis set uses an energy cut-off of 500 eV, and the Brillouin zone is sampled using  $8 \times 8 \times 8$  k-points for all calculations. The application of the Broyden has optimized the geometric structure using the Fletcher–Goldfarb–Shanno (BFGS) minimization technique<sup>40</sup>. The adopted Hubbard parameter  $U = 2.5$  eV for the Cr 3d orbitals is consistent with previously reported DFT+U studies on chromium-based compounds, where comparable values  $U = 2.5$  eV for Cr in chromium carbides have been successfully employed to describe the localized 3d electrons of  $Cr^{41}$ . The Vanderbilt-type ultrasoft pseudopotential (UPP) formalism was used to analyze the interactions between valence electrons and ions. UPPs achieve a substantially softer pseudo-wave function, requiring a significant reduction in plane waves for



calculations with the same level of precision<sup>42</sup>. Additionally, spin polarization was only applied to the magnetic state material in the comparison material used in the lowest energy computation, and spin polarization was not applied to the non-magnetic state material in all other computations. The elastic constants were determined using first-principles computations by carrying out a sequence of specified homogeneous distortions with finite parameters and calculating the resulting stress concerning optimizing the interior atomic freedom. With an upper limit of 0.5%, each strain element had three positive and three negative amplitudes. After that, the calculated stress as a function of strain was fitted linearly to obtain the parameters of the elastic modulus. To facilitate the calculation of the optical properties for a dense mesh of evenly distributed k-points, the BZ integration was performed using a  $12 \times 12 \times 12$  MP k-mesh.

**Table I:** A summary of the chosen parameters for the DFT-calculations performed in the present work.

Category	Cubic
Values of Descriptions	
<b>Convergence</b>	Energy tolerance: $1.0 \times 10^{-6}$ a.u.; Force tolerance: $1.0 \times 10^{-4}$ a.u.
<b>Exchange-correction functionals</b>	PBE-GGA(Perdew–Burke–Ernzerhof), GGA-PBEsol and GGA+U
<b>Plane-wave cutoffs</b>	500 eV
<b>Smearing section</b>	Occupations = smearing; Method = Gaussian; Width = 0.10 eV
<b>K-points Grid</b>	$8 \times 8 \times 8$
<b>Pseudopotentials</b>	OTFG ultrasoft
<b>Relativistic treatment</b>	Koelling–Harmon
<b>Spin treatment</b>	Spin Polarized (FM calculations)
<b>Electronic minimization</b>	Metallic treatment with density mixing; Pulay mixing scheme
<b>Geometry optimization</b>	Method = BFGS; Max steps = 1000; Force tolerance = $0.05 \text{ eV}/\text{\AA}$ ; Stress tolerance = 0.1 GPa



### 3.1 Structural Properties and Structural Stability

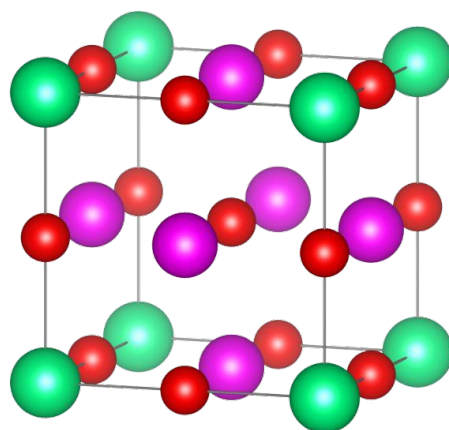
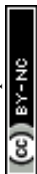


**Figure 1:** Crystal structure of cubic  $A_3CrO_4$  compounds ( $A = Mg, Ca, Sr$ ).

$A_3CrO_4$  ( $A = Mg, Ca, Sr$ ) is structured in the cubic  $P\bar{m}3m$  space group shown in **Figure 1**. The Wyckoff positions  $3c$  ( $0, \frac{1}{2}, \frac{1}{2}$ ),  $1a$  ( $0, 0, 0$ ),  $3d$  ( $0, 0, \frac{1}{2}$ ) and  $1b$  ( $\frac{1}{2}, \frac{1}{2}, \frac{1}{2}$ ) in this crystal structure are occupied by A, B, O1 and O2 atoms, respectively<sup>43</sup>. These structures are optimized in ferromagnetic (FM) and non-magnetic (NM) states to verify the most stable state. The Birch-Murnaghan equation of state (EOS) is a fundamental model used to describe the pressure-volume relationship of materials, particularly under high-pressure conditions, by expanding the solid's free energy as a polynomial in the Eulerian finite strain. While the standard third-order Birch-Murnaghan EOS is well-defined for cubic materials<sup>44</sup>. The present materials were simulated in FM and NM magnetic configurations in various exchange functional to extract the ground state structural parameters by performing a least-squares fit of the crystal energy against the unit cell volume through the Birch-Murnaghan equation of state<sup>45</sup>,

$$E(V) = E_0 + \left(\frac{9B_0V_0}{16}\right) \left\{ \left[ \left(\frac{V_0}{V}\right)^{\frac{2}{3}} - 1 \right] B'_0 + \left[ \left(\frac{V_0}{V}\right)^{\frac{2}{3}} - 1 \right]^2 \left[ 6 - 4 \left(\frac{V_0}{V}\right)^{\frac{2}{3}} \right] \right\} \quad (1)$$

The terms  $E(V)$ ,  $V$  and  $B_0$  ( $B'_0$ ) in this equation represents the ground state energy, unit cell volume, and the bulk modulus (pressure derivate of the bulk modulus), respectively. For all the compounds the optimized energy-volume curve in these different phases clearly indicates that FM



phase is significantly most stable as it holds lowest energy in all approximation rather than NM phase as depicted in **Figure 3(a-i)**.

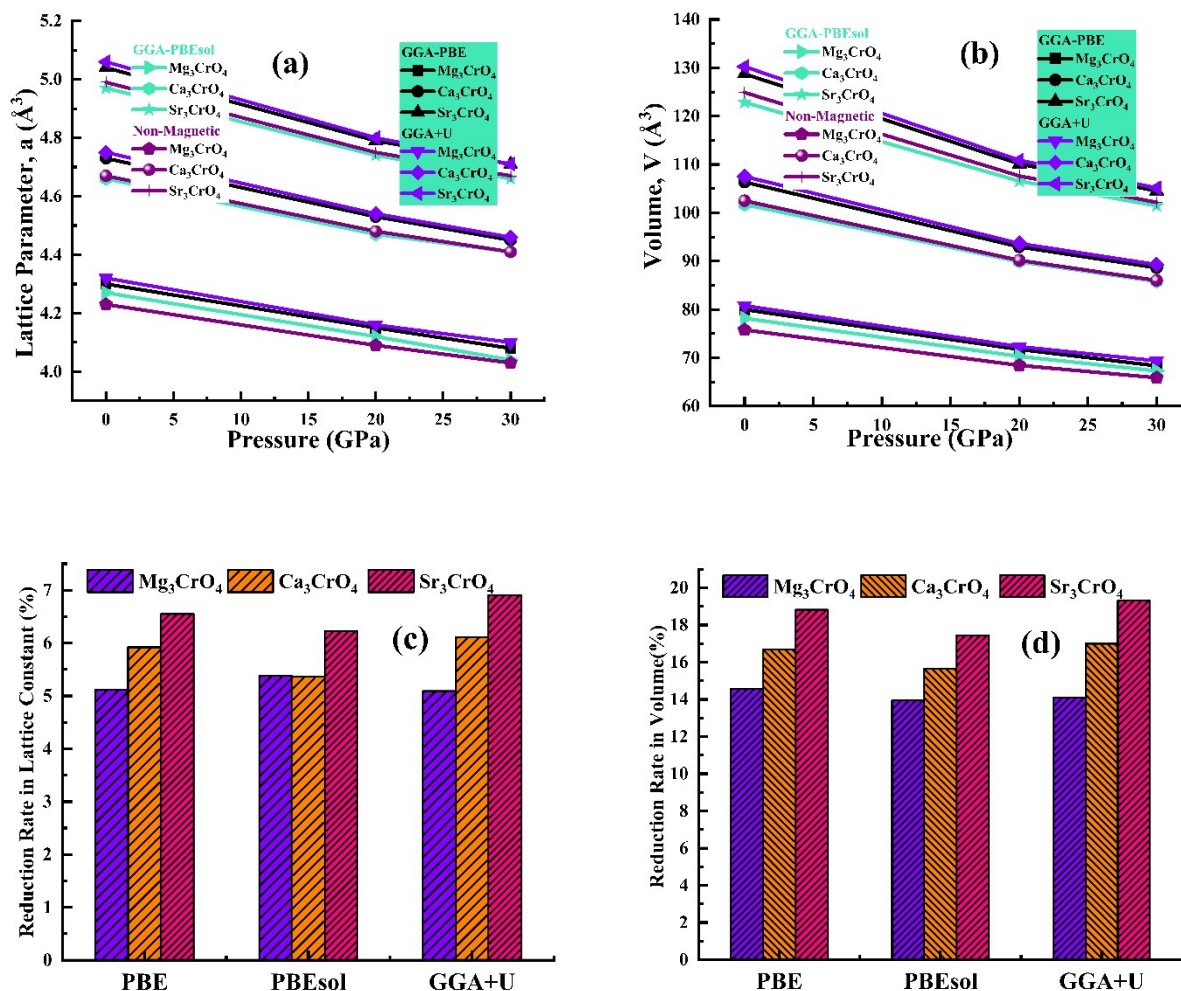


**Figure 2:** Change in lattice parameter and volume of cubic  $A_3CrO_4$  compounds ( $A = Mg, Ca, Sr$ ) under pressure (0–30 GPa) with different functionals.

Variations in lattice parameters arise from the distinct treatment of the exchange-correlation term by different functionals. Hence,  $A_3CrO_4$  ( $A = Mg, Ca, Sr$ ) was geometrically optimized with GGA-PBE, GGA+U and GGA-PBEsol functionals and value reported in **Table III**. As shown in Figure 2(a-b), hydrostatic pressure strongly influences the lattice parameters, unit cell volumes across PBE, PBEsol and GGA+U calculations. Increasing pressure gradually reduces the lattice



parameters by shortening interatomic distances. From Figure 2(c), the lattice constant reduction are modest with GGA-PBEsol consistently predicting slightly lower compressibility relative to GGA-PBE and GGA+U. In Figure 2(d) the volume reduction are significantly higher across all functional. This comparative analysis highlights that while lattice constants provide a direct measure of contraction, volume reductions offer a more sensitive indicator of bulk compressibility, and functional choice introduces systematic variations that must be considered in high-pressure predictions.

**Table II:** Ground-state structural parameters of  $A_3CrO_4$  ( $A = Mg, Ca, Sr$ ): lattice constant ( $a$ , Å), volume ( $V$ , Å<sup>3</sup>), crystal energy ( $E_0$ , eV), bulk modulus ( $B$ , GPa) and tolerance factor ( $t$ ) under pressure 0-30GPa.

		$Mg_3CrO_4$			$Ca_3CrO_4$			$Sr_3CrO_4$		
		0 GPa	20-GPa	30-GPa	0 GPa	20-GPa	30-GPa	0 GPa	20-GPa	30-GPa
GGA-PBE(FM- State)	Lattice Constant $a$ (Å)	4.30	4.15	4.08	4.73	4.53	4.45	5.04	4.79	4.71
	Volume $V$ (Å <sup>3</sup> )	79.98	71.76	68.36	106.36	92.96	88.64	128.75	110.12	104.52
	Energy $E$ (eV)	-	-	-9238.86	-7183.08	-7182.47	-7181.82	-6798.26	-6797.44	-6796.50
	Bulk Modulus $B$ (GPa)	124.14	156.87	228.97	97.95	278.87	418.62	90.50	232.08	371.48
PBE(NM- State)	Lattice Constant $a$ (Å)	-9238.4	-	-9237.64	-7181.15	-7180.59	-7179.97	-6795.90	-6795.21	-6794.39
	Volume $V$ (Å <sup>3</sup> )	4.23	4.09	4.03	4.67	4.48	4.41	4.99	4.75	4.67
	Energy $E$ (eV)	75.77	68.45	65.89	102.48	90.18	86.02	124.88	107.64	102.15
	Bulk Modulus $B$ (GPa)	96.82	536.12	815.04	140.92	232.05	338.43	68.32	227.22	368.05
	<b>Tolerance Factor</b>	0.82			0.92			0.99		
Other Calculation		$Mg_3FeO_4$			$Ca_3FeO_4$			$Sr_3FeO_4$		
	Lattice Constant $a$ (Å)	4.28 <sup>46</sup>			4.74 <sup>46</sup>			5.03 <sup>46</sup>		
	Energy $E$ (Ry)	-4350.39 <sup>46</sup>			-7230.82 <sup>46</sup>			-22227.41 <sup>46</sup>		
	Bulk Modulus $B$ (GPa)	152.003 <sup>46</sup>			108.95 <sup>46</sup>			94.36 <sup>46</sup>		

Any deviance from the optimal cubic structure can be assessed by the tolerance factor ( $t$ ) that typically ranges from 0.81 to 1.11 for cubic perovskites<sup>47</sup>. The Goldschmidt tolerance factor,  $t$  is given as,

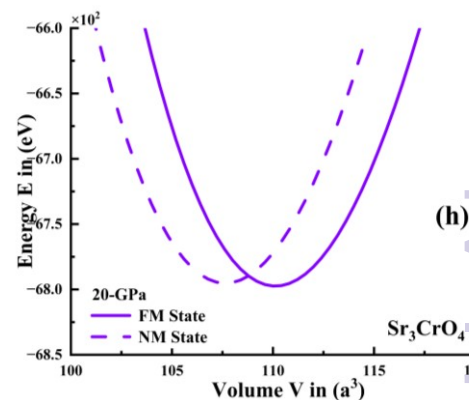
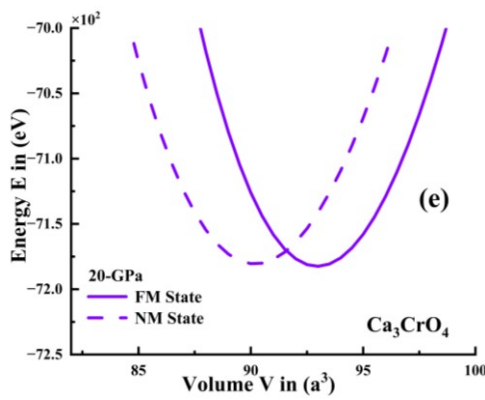
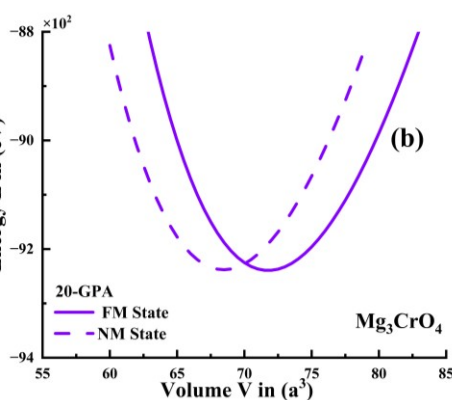
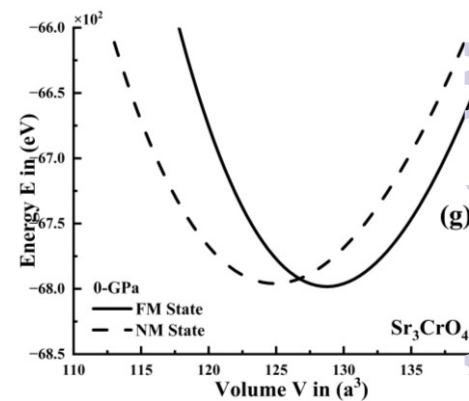
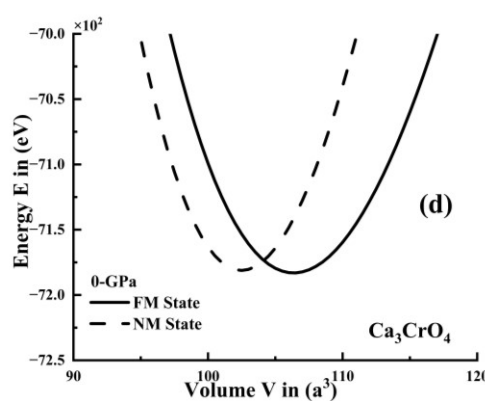
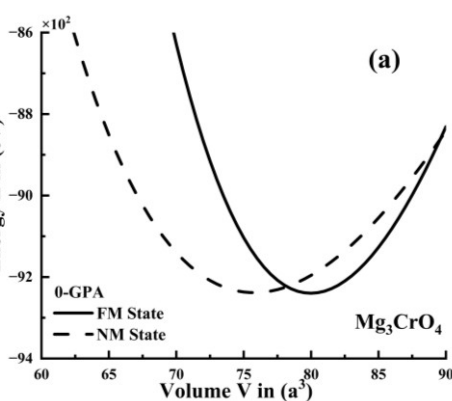
$$t = 0.707 \frac{r_A + r_O}{\{r_{Cr} + r_O\}} \quad (2)$$

Where  $r_A$ ,  $r_O$ ,  $r_{Cr}$  represents the atomic radius of the A-site atom (A=Mg, Ca, Sr), O atom, and Cr atom, respectively, which are calculated by using Shannon's effective ionic radii and the values  $t$  of these are depicted in **Table II**. Deviation of the tolerance factor from unity reduces the likelihood of stabilizing a cubic phase and instead favors the formation of less symmetric structures. The calculated  $t$ -values for  $A_3CrO_4$  (A = Mg, Ca, Sr) perovskites (Table 1) confirm the stability of the cubic structure.

Open Access Article. Published on 27 April 2026. Downloaded on 5/21/2026 7:40:38 PM.  
This article is licensed under a Creative Commons Attribution-NonCommercial 3.0 Unported Licence.



Energy E<sub>i</sub> in (eV)



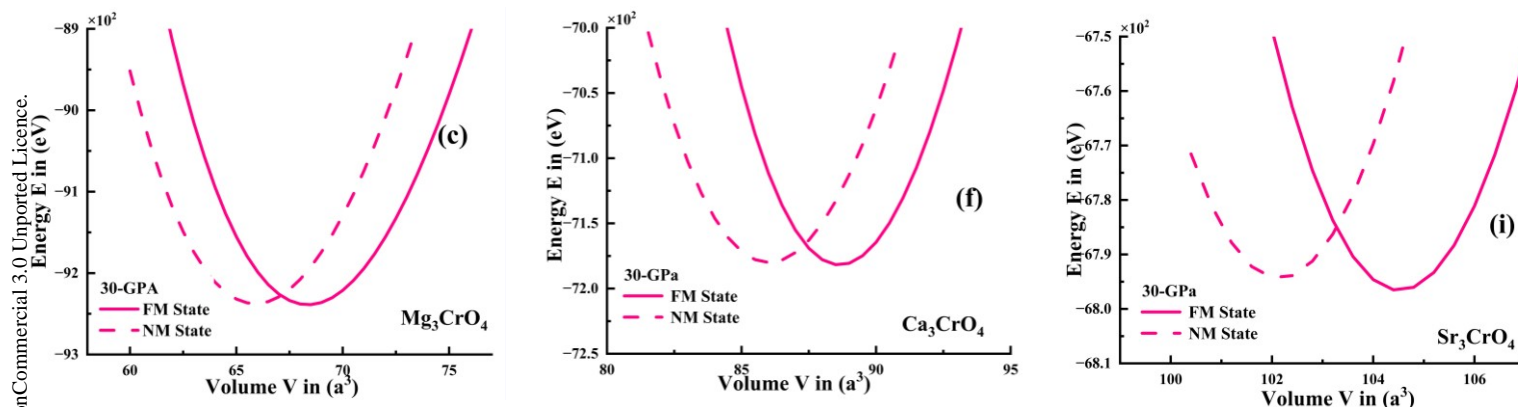


**Figure 3:** Energy versus Volume curve (a-i) for  $A_3CrO_4$  compounds ( $A = Mg, Ca, Sr$ ) under hydrostatic pressures (0–30 GPa) for FM (ferromagnetic) and NM (non-magnetic state).

**Table III:** Percentage reduction in lattice constant ( $a$ , Å) and unit cell volume ( $V$ , Å<sup>3</sup>) for  $Mg_3CrO_4$ ,  $Ca_3CrO_4$  and  $Sr_3CrO_4$  from 0 to 30 GPa calculated using different functionals.

Dependence	Lattice Constant Reduction in %	$Mg_3CrO_4$			$Ca_3CrO_4$			$Sr_3CrO_4$		
		GGA-PBE	GGA-PBEsol	GGA+U	GGA-PBE	GGA-PBEsol	GGA+U	GGA-PBE	GGA-PBEsol	GGA+U
		5.12	5.38	5.09	5.92	5.36	6.11	6.55	6.23	6.91
Volume Reduction in %	Volume Reduction in %	GGA-PBE	GGA-PBEsol	GGA+U	GGA-PBE	GGA-PBEsol	GGA+U	GGA-PBE	GGA-PBEsol	GGA+U
		14.56	13.94	14.11	16.67	15.65	16.99	18.82	17.44	19.31

## 3.2 Electronic Properties

After completing the geometric optimization of  $A_3CrO_4$  compounds ( $A = Mg, Ca, Sr$ ) under hydrostatic pressures (0–30 GPa), it is crucial to analyze their electronic structures to determine whether they exhibit half-metallic characteristics and to assess their suitability for photoelectric and optoelectronics applications<sup>48</sup>. Band structure and density of states (DOS) calculations provide essential insights into electron dispersion, band gap properties and orbital contributions that influence optical absorption, carrier transport and radiative efficiency<sup>49</sup>.

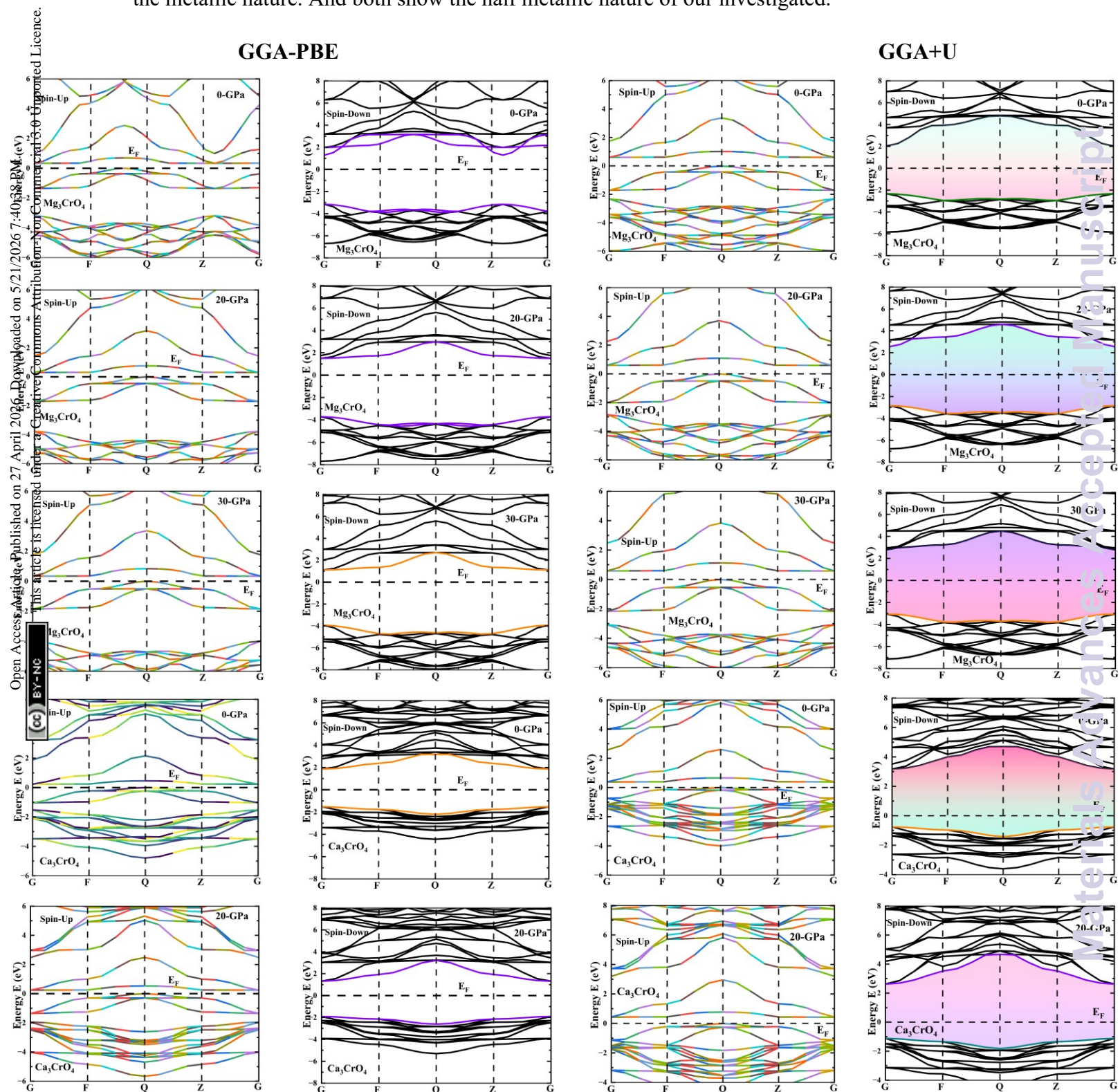
**Figure 4** illustrates the band structures of  $A_3CrO_4$  compounds ( $A = Mg, Ca, Sr$ ) obtained using two different exchange-correlation functionals along high-symmetry paths. Across the entire pressure range (0-30) GPa, the spin down channel shows wide semiconducting band gap. In



contrast in the spin up channel the valance conduction band merge in the Fermi level confirming the metallic nature. And both show the half metallic nature of our investigated.

## GGA-PBE

## GGA+U



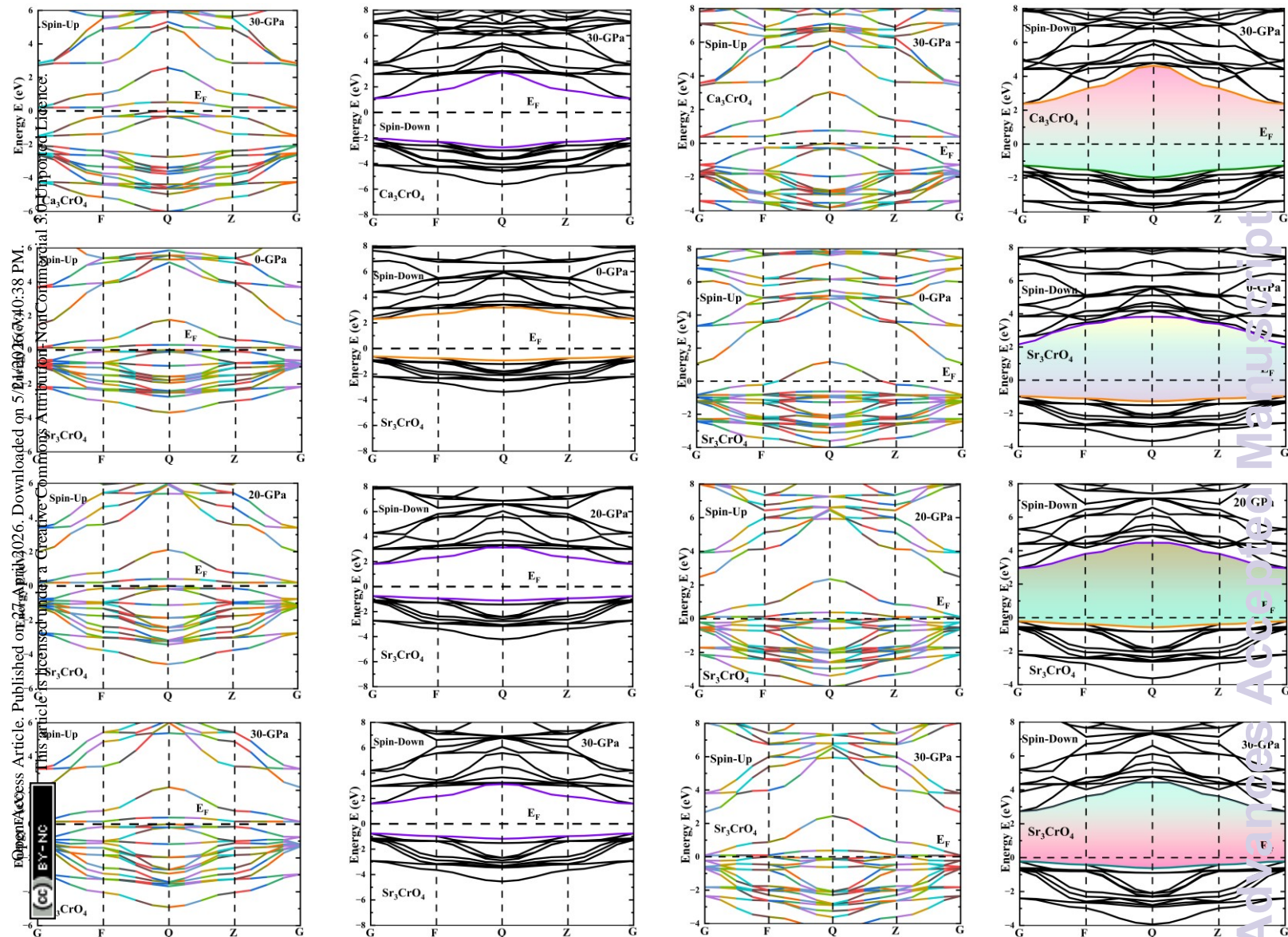


**Figure 4:** Band structure of  $A_3CrO_4$  compounds ( $A = Mg, Ca, Sr$ ) under hydrostatic pressures (0–30 GPa) for GGA-PBE and GGA+U functionals.

When the Hubbard correction GGA+U is applied, the band gap increases reflecting the tendency of semi-local GGA to underestimate band gaps and improved accuracy of GGA+U. The systematic increase in band-gap values from GGA-PBE to GGA+U highlights the intrinsic limitation of semi-local functionals in underestimating band gaps because of the absence of derivative discontinuity in the exchange potential<sup>50</sup>. The consistent GGA/GGA+U trend observed here confirms the robustness of the electronic structure calculations and supports the reliability of the predicted half metallic behavior of  $A_3CrO_4$  compounds ( $A = Mg, Ca, Sr$ ) and hybrid functionals



provide more accurate band-gap estimations, they are computationally demanding, making them less practical for large-scale property calculations on standard computing platforms. In contrast, GGA-PBE offers a good balance between efficiency and accuracy, and thus was used for all subsequent calculations, while GGA+U was employed primarily for band-gap correction and validation.

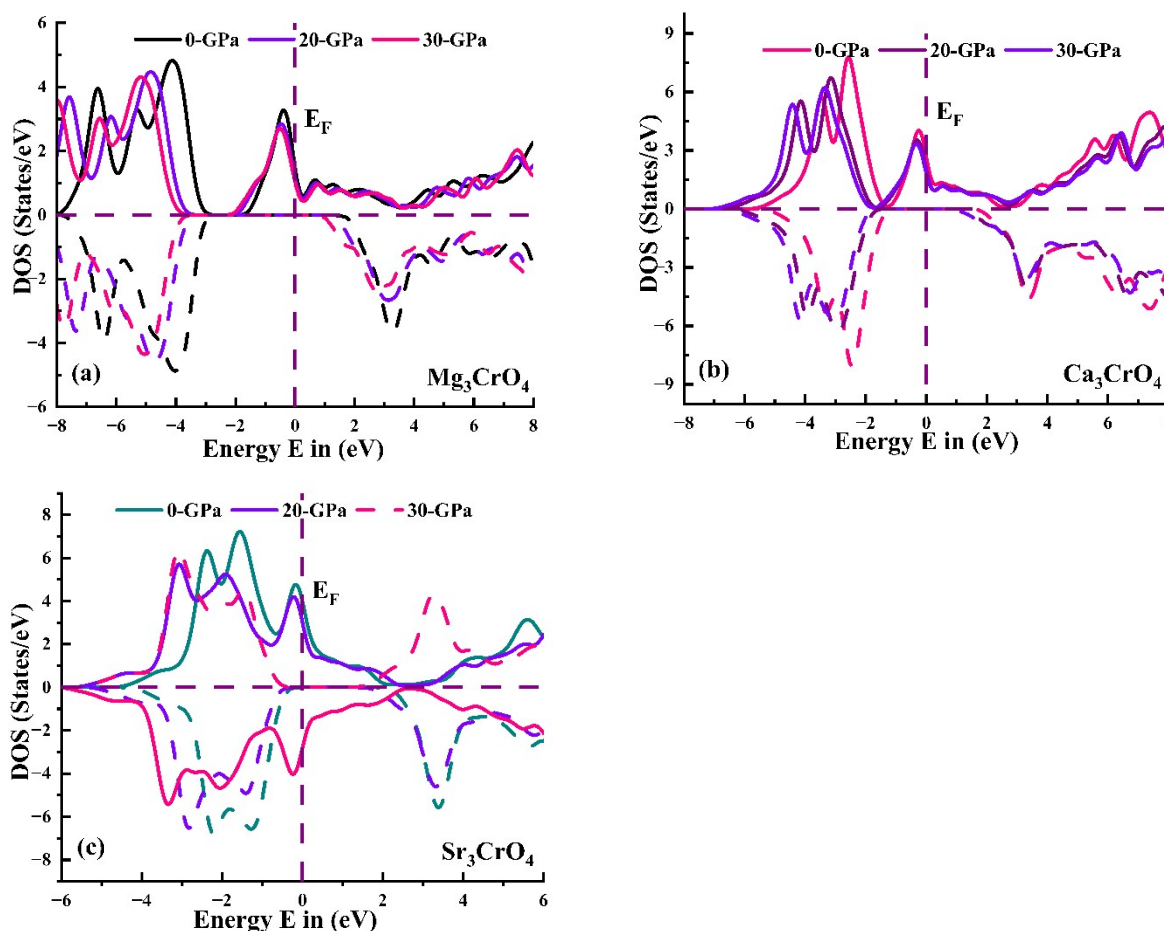


**Figure 5:** Total density of states (TDOS) of  $A_3CrO_4$  compounds ( $A = Mg, Ca, Sr$ ) under hydrostatic pressures (0–30 GPa).

The total density of states (TDOS) describes the distribution of electronic energy levels per unit interval and serves as a key indicator of the overall electronic structure of a material<sup>51</sup>. **Figure 5** shows the TDOS of  $A_3CrO_4$  compounds calculated using the GGA functional. All investigated systems exhibit ferromagnetic ground states across the studied pressure range, where the spin-up channel behaves metallic and the spin-down channel semiconducting, except for  $Sr_3CrO_4$  at 30 GPa, where the characteristics are reversed, confirming its antiferromagnetic nature as evidenced



by the Fermi level position. The unequal contributions from the two spin channels further validate their magnetic behavior. In addition, the TDOS reveals the band gaps of these compounds, which are consistent with the corresponding band structure results.

### 3.3 Spin Magnetic Moments

At  $T = 0$  K, the spin-polarized computation directly obtains the magnetic moment. Utilizing the actual magnetic moments per formula unit, the magnetic moment is calculated as follows,

$$\mu = 4\mu_{\text{oxygen}} + \mu_{\text{Cr}} + 3\mu_{\text{(Mg, Ca, Sr)}} \quad (3)$$

The **Table IV** provide the spin magnetic moments  $\mu_B$  for A-site cations ( $A = \text{Mg, Ca, Sr}$ ), Chromium (Cr) and Oxygen (O) anions in the  $A_3\text{CrO}_4$  family under varying hydrostatic pressures (0, 20, 30 GPa) and using three distinct functionals GGA-PBE, GGA-PBESol and GGA+U. These calculations provide critical insights into the magnetic behavior of these chromate perovskite-related materials and their potential for spintronic applications, especially under pressure-induced modifications. Understanding these properties is vital for the design of materials with tunable magnetic responses<sup>52,53</sup>. For Mg and Ca based compounds the data consistently indicate a ferromagnetic (FM) alignment with positive total magnetic moments approximately  $+4\mu_B$  to  $+4.1\mu_B$  observed across all pressures and DFT functionals. This behavior is consistent with  $\text{Cr}^{3+}(\text{d}^3, \text{high-spin}, S=3/2)$  ions, where the magnetic moments of the Cr and O atoms align to produce a net ferromagnetic state. Such ferromagnetic coupling in chromite's is often mediated by superexchange interactions and hybridization effects<sup>54-56</sup>. The A-site cations (Mg and Ca) exhibit small positive magnetic moments, while the Cr ions contribute the dominant positive moment, generally ranging from  $3.18\mu_B$  to  $3.78\mu_B$ . depending on the specific compound, pressure and functional. The oxygen anions also contribute positive moments, suggesting a degree of spin polarization induced by their interaction with the Cr ions.

In contrast  $\text{Sr}_3\text{CrO}_4$  exhibits a notable and intriguing pressure-induced magnetic transition. At 0-GPa, under GGA-PBE functional  $\text{Sr}_3\text{CrO}_4$  shows a positive total magnetic moment approximately  $+4\mu_B$ . However, as pressure increase to 20GPa and further to 30GPa, the total magnetic moments reverse sign, becoming approximately  $-4\mu_B$  and  $-4.01\mu_B$  respectively under GGA-PBE and GGA-PBESol functionals demonstrated in **Figure-6**. This sign reversal suggests a shift from an initial ferromagnetic ordering to an antiferromagnetic (AFM) or ferrimagnetic



ordering where the dominate magnetic moments align antiparallel to their initial orientation<sup>57</sup>. This transition is particularly significant as it implies that the magnetic properties of  $\text{Sr}_3\text{CrO}_4$  can be manipulated by external pressure, offering potential avenues for mechanically controlled spin or switchable spintronics materials<sup>58</sup>. Such pressure-driven transitions have been observed in other transition metal oxides, impacting their electronic and magnetic structures<sup>54,59</sup>. The phenomenon in  $\text{Sr}_3\text{CrO}_4$ , is similar of pressure-induced spin-state transitions in iron-based oxides, which can lead to novel functionalities<sup>60</sup>.

**Table-IV:** The calculated magnetic moments  $\mu_B$  for cubic  $\text{A}_3\text{CrO}_4$  compounds (A = Mg, Ca, Sr) under hydrostatic pressures (0–30 GPa) using different exchange correlation functionals.

		$\text{Mg}_3\text{CrO}_4$			$\text{Ca}_3\text{CrO}_4$			$\text{Sr}_3\text{CrO}_4$		
		0-GPa	20-GPa	30-GPa	0-GPa	20-GPa	30-GPa	0-GPa	20-GPa	30-GPa
GGA-PBE	$\mu_A$	0.21	0.21	0.21	0.24	0.30	0.30	0.27	-0.27	-0.30
	$\mu_{\text{Cr}}$	3.52	3.45	3.18	3.64	3.53	3.48	3.79	-3.64	-3.59
	$\mu_O$	0.36	0.44	0.44	0.12	0.24	0.28	-0.08	-0.08	-0.12
	$\mu_{\text{Total}}$	4.09	4.10	3.83	4.00	4.07	4.06	4.00	-3.99	-4.01
GGA-PBESol	$\mu_A$	0.21	0.21	0.18	0.27	0.30	0.30	-0.27	-0.30	-0.33
	$\mu_{\text{Cr}}$	3.50	3.27	3.06	3.60	3.48	3.37	-3.74	-3.60	-3.56
	$\mu_O$	0.36	0.44	0.44	0.16	0.28	0.28	0.04	-0.12	-0.16
	$\mu_{\text{Total}}$	4.07	3.92	3.68	4.03	4.06	3.95	-3.97	-4.02	-4.05
GGA-GGA+U	$\mu_A$	0.21	0.21	0.24	0.27	0.30	0.30	0.27	0.30	0.30
	$\mu_{\text{Cr}}$	3.63	3.54	3.50	3.78	3.65	3.61	3.96	3.78	3.74
	$\mu_O$	0.20	0.32	0.36	0.08	0.04	0.08	-0.32	-0.12	-0.08
	$\mu_{\text{Total}}$	4.04	4.07	4.10	4.13	3.99	3.99	3.91	3.96	3.96

In **Table IV**, GGA+U generally yields more stable positive magnetic moments for all compounds with the total magnetic moments consistently around  $+4\mu_B$  to  $+4.1\mu_B$ . This suggests that the on-site Coulomb correction stabilizes the high spin  $d^3$  state of  $\text{Cr}^{3+}$  making it less susceptible to charge transfer effects or spin collapse under pressure<sup>61,62</sup>. For  $\text{Sr}_3\text{CrO}_4$ , while PBE and PBESol show a moment reversal, GGA+U consistently maintains a positive magnetic moment across all pressures indicating a more robust ferromagnetic state predicted by this functional. This



highlights the importance of accurately treating electron corrections in such systems, as the magnetic ground state can be sensitive to the chosen theoretical framework.

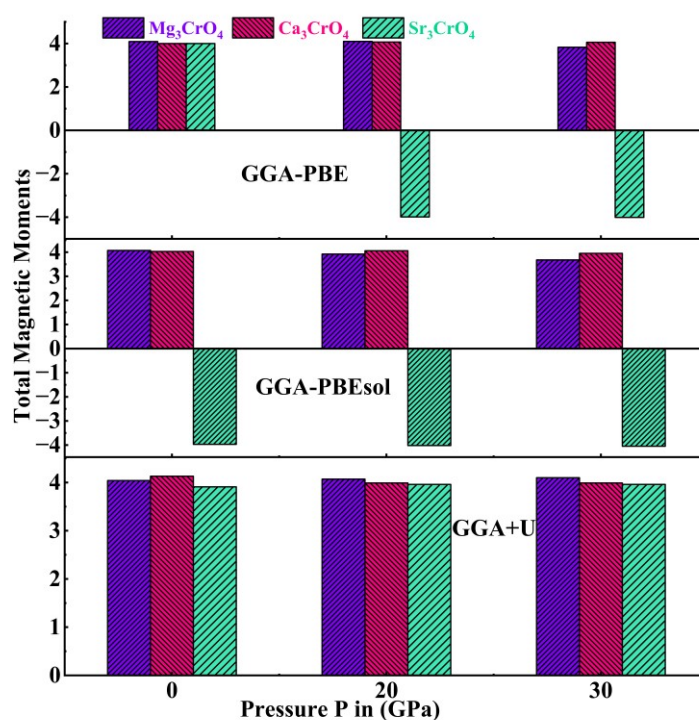


**Figure-6:** The magnetic moments  $\mu_B$  for cubic  $A_3CrO_4$  compounds ( $A = Mg, Ca, Sr$ ) under hydrostatic pressures (0–30 GPa) using different exchange correlation functionals.

The oxygen anion moments provide further insights into the electron structure and bonding. In  $Mg_3CrO_4$  and  $Ca_3CrO_4$  the positive oxygen moments increase with pressure under GGA-PBE and GGA-PBEsol. This increase reflects enhanced covalency and p-d hybridization between oxygen and chromium under compression. Similar observations have been made in other transition-metal oxides like NiO and CoO where pressure strengthens the hybridization between oxygen 2p and transition metal 3d orbitals leading to greater spin polarization of the oxygen sublattice<sup>63</sup>.

In  $Sr_3CrO_4$  however the oxygen moments also reverse sign under PBE and PBEsol with increasing pressure, aligning with the overall change in the total magnetic moment. This suggests that the oxygen sublattice actively participated in the pressure-induced magnetic transition, rather than merely reflecting the Cr moments. The magnetic properties of Cr-containing perovskites are generally complex due to the competition between direct exchange and superexchange interactions and the influence of the structural distortions<sup>64–67</sup>.



Overall, materials with tunable spin polarization could be employed in pressure-sensitive magnetic sensors, data storage devices, spin valves where mechanical strain dictates magnetic state<sup>68,69</sup>

### 3.4 Elastic Properties and Dynamical Stability

Elastic constants are necessary to have a more thorough theoretical comprehension of the characteristics of materials that are determined by the electron-phonon interaction processes and the density of states of phonons. Since the stress-strain curve in many minerals exhibits low nonlinearity, practical applications can assume a linear relationship between stress and strain<sup>70</sup>. Elastic constants can calculate essential physical parameters like melting point, hardness, sound velocities, Debye temperature, and shear modulus. The elastic constants are the total energy second derivative for different lattice deformations. More thorough computations of the total energy are necessary<sup>71</sup> for the elastic constants. The elastic constants can be calculated from the resulting formula,

$$C_{ij} = \frac{1}{V_0} \left( \frac{d^2 E}{de_i e_j} \right) \quad (4)$$

E is the internal energy,  $V_0$  indicate equilibrium volume and  $e_i$  and  $e_j$  is the stress and strain components.

Since  $A_3CrO_4$  ( $A = Mg, Ca, Sr$ ) is a cubic structure with a high degree of symmetry, the elastic constant reduces to three independent elastic constants:  $C_{11}$ ,  $C_{12}$ , and  $C_{44}$ <sup>72</sup> reported in **Table-V**. The following is an expression of the conventional mechanical stability conditions in cubic crystals at equilibrium in terms of elastic constants<sup>73,74</sup>,

$$C_{44} > 0, C_{11} > |C_{12}|, C_{11} + 2C_{12} > 0 \quad (5)$$

The equations for mechanical stability under pressure are given by<sup>75</sup>,

$$C'_{11} - C'_{12} = (C_{11} - C_{12}) - 2P > 0, C'_{11} + 2C'_{12} = (C_{11} + 2C_{12}) > 0, C'_{44} = C_{44} - P > 0 \quad (6)$$

As reported in **Table-VI**, all investigated compounds satisfy both the Born and dynamical stability criteria, thereby confirming their reliability under the studied conditions.

The formulations associated with the calculations of Bulk modulus(B), Shearing modulus(G), Young's modulus(E), Anisotropy(A), Poisson's ratio( $\nu$ ), Pugh's ratio(B/G), plasticity



measurement( $B/C_{44}$ ), Kleinman parameter ( $\zeta$ ) have been computed using the following are given by the following expressions, respectively <sup>76-80</sup>,

$$B = \frac{1}{3}(C_{11} + 2C_{12}) \quad (7)$$

$$G = \frac{G_V + G_R}{2} \quad (8)$$

$$G_V = \frac{C_{11} - C_{12} + C_{44}}{5} \quad (9)$$

$$G_R = \frac{5C_{44}(C_{11} - C_{12})}{4C_{44} + 3(C_{11} - C_{12})} \quad (10)$$

$$E = \frac{9BG}{(3B + G)} \quad (11)$$

$$A = \frac{2C_{44}}{C_{11} - C_{12}} \quad (12)$$

$$v = \frac{(3B - 2G)}{2(3B + G)} \quad (13)$$

$$\zeta = \frac{C_{11} + 8C_{12}}{7C_{11} + 2C_{12}} \quad (14)$$

**Table V:** Pressure-dependent mechanical stability conditions for  $A_3CrO_4$  ( $A = Mg, Ca, Sr$ ).

Compounds	Pressure P	Born Stability at P=0(GPa)			Dynamical Stability			Stability
		$C_{11}$	$C_{44}$	$C_{11} + 2C_{12}$	$C'_{11} - C'_{12}$	$C'_{11} + 2C'_{12}$	$C'_{44}$	Stable
$Mg_3CrO_4$	<b>0-GPa</b>	239.07	110.75	447.29	134.96	447.29	110.75	<b>Stable</b>
	<b>20-GPa</b>	343.78	114.08	492.88	249.68	492.88	94.08	<b>Stable</b>
	<b>30-GPa</b>	478.14	117.29	680.70	245.58	680.70	87.29	<b>Stable</b>
$Ca_3CrO_4$	<b>0-GPa</b>	214.37	74.05	339.65	151.73	339.65	74.05	<b>Stable</b>
	<b>20-GPa</b>	391.87	72.90	581.09	183.66	581.09	52.90	<b>Stable</b>
	<b>30-GPa</b>	466.44	74.19	657.38	245.97	657.38	44.19	<b>Stable</b>
$Sr_3CrO_4$	<b>0-GPa</b>	177.63	53.55	273.53	129.68	273.53	53.55	<b>Stable</b>
	<b>20-GPa</b>	362.99	48.90	529.83	176.15	529.83	28.90	<b>Stable</b>
	<b>30-GPa</b>	444.05	42.07	638.57	219.53	638.57	12.07	<b>Stable</b>

The elastic constants  $C_{11}$ ,  $C_{12}$  and  $C_{44}$  provide fundamental insights into the materials response to external stress. For all three investigating compounds  $C_{11}$  significantly increase with pressure shown in **Figure 7(a)** indicating enhanced resistance to uniaxial compression. This trend is typical for solids under pressure, as interatomic distances decrease, leading to stronger bonds and a stiffer



lattice<sup>81</sup>. The increase in  $C_{12}$  and  $C_{44}$  also suggests increased resistance to shear deformation and improved shear stiffness under compression. The positive values of elastic constants across all the pressure satisfied Born stability criteria of these cubic structures under the investigated conditions.

**Table-VI:** The calculated elastic constants  $C_{ij}$  (GPa), bulk modulus  $B$  (GPa), shear modulus  $G$  (GPa), Young's modulus  $Y$  (GPa), Pugh's ratio  $G/B$ , Poisson's ratio ( $\nu$ ) of  $A_3CrO_4$  compounds ( $A = Mg, Ca, Sr$ ) under hydrostatic pressures 0–30 GPa.

		$Mg_3CrO_4$			$Ca_3CrO_4$			$Sr_3CrO_4$		
		0-GPa	20-GPa	30-GPa	0-GPa	20-GPa	30-GPa	0-GPa	20-GPa	30-GPa
<b>Elastic Constants</b>	$C_{11}$ (GPa)	239.07	343.78	478.14	214.37	391.87	466.44	177.63	362.99	444.05
	$C_{12}$ (GPa)	104.11	74.55	101.28	62.64	94.61	95.47	47.95	83.42	97.26
	$C_{44}$ (GPa)	110.75	114.08	117.29	74.05	72.90	74.19	53.55	48.90	42.07
	<b>Bulk Modulus B (GPa)</b>	149.09	164.29	226.9	113.21	193.69	219.12	71.17	176.61	212.85
	<b>Poisson Ratio <math>\nu</math></b>	0.24	0.20	0.24	0.22	0.284	0.288	0.23	0.31	0.37
	<b>Shear Modulus G (GPa)</b>	90.79	121.89	141.94	74.77	97.37	108.16	45.07	75.67	77.47
	<b>Young Modulus Y (GPa)</b>	226.41	293.17	352.36	183.84	250.20	278.64	111.65	198.64	207.28
	<b>Anisotropy factor A</b>	0.30	0.84	0.62	0.97	0.49	0.39	1.53	0.34	0.24
	<b>Pugh Ratio B/G</b>	1.64	1.34	1.59	1.51	1.98	2.02	1.57	2.33	2.74
	<b>Kleinman Parameter</b>	0.56	0.36	0.36	0.44	0.39	0.35	0.54	0.38	0.37
	<b>Nature</b>	Brittle	Brittle	Brittle	Brittle	Ductile	Ductile	Brittle	Ductile	Ductile
	<b>Other Calculation<sup>46</sup></b>	$Mg_3FeO_4$			$Ca_3FeO_4$			$Sr_3FeO_4$		
	$C_{11}$	254.61			244.81			181.69		
	$C_{12}$	102.51			57.60			51.81		
	$C_{44}$	117.35			101.21			88.62		
	<b>Bulk Modulus B (GPa)</b>	153.21			120.01			95.10		
	<b>Poisson Ratio <math>\nu</math></b>	0.23			0.17			0.17		
	<b>Shear Modulus G (GPa)</b>	98.62			98.09			78.24		
	<b>Anisotropy factor A</b>	1.54			1.08			1.36		
	<b>Pugh Ratio B/G</b>	1.53			1.22			1.21		
	<b>Kleinman Parameter</b>	0.54			0.38			0.43		
	<b>Nature</b>	Brittle			Brittle			Brittle		

The bulk modulus representing resistance to volume change, consistently increase with pressure for all the compounds shown in **Figure 7(c)**. This indicates that all three compounds become significantly stiffer and less compressible under elevated pressure. The Young's modulus which measures stiffness also increases with pressure, reinforcing the observation of enhanced mechanical rigidity. Among the investigated compounds  $Mg_3CrO_4$  compounds dominant all the pressure range shown in **Figure 7(b)**. These findings suggest that these chromates could



potentially maintain their structural integrity in high-pressure environments making them candidates for applications requiring mechanically robust materials<sup>60</sup>.

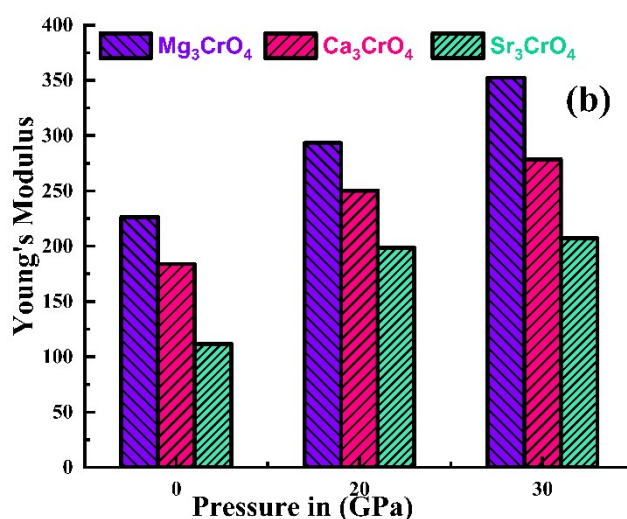
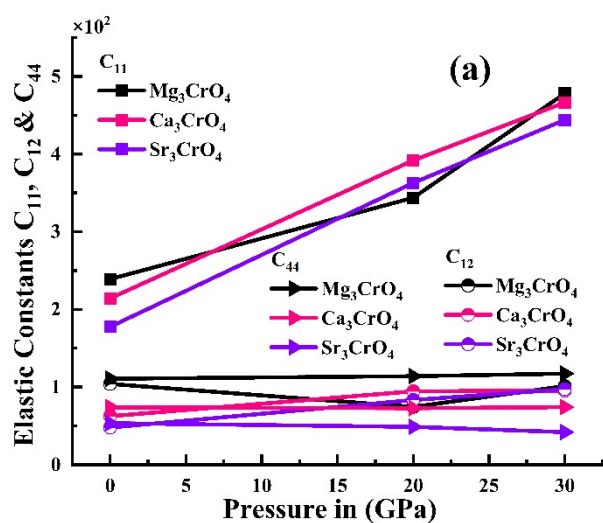
Poisson's ratio, an elastic constant that describes how a material deforms sideways in response to longitudinal force, is also known as the transverse deformation coefficient. Poisson's ratio is a characteristic with a minimum value of approximately 0.26<sup>82</sup> in most metals. A Poisson's ratio greater than 0.25 suggests predominantly ionic bonding in the compound, whereas a value below 0.25 indicates predominantly covalent bonding<sup>83</sup>. The Poisson's ratio values indicate that  $\text{Mg}_3\text{CrO}_4$  ( $\nu < 0.25$ ) exhibits predominantly covalent bonding, whereas  $\text{Ca}_3\text{CrO}_4$  and  $\text{Sr}_3\text{CrO}_4$  ( $\nu > 0.25$  at higher pressures) show a transition toward ionic bonding character, consistent with their enhanced ductility under compression. For  $\text{Mg}_3\text{CrO}_4$ , Poisson's ratio fluctuates between 0.20 and 0.24 suggesting it remains relatively brittle.  $\text{Ca}_3\text{CrO}_4$  shows an increase from 0.22 to 0.288 indicating a potential shift towards more ductile behavior at higher pressures. Notably,  $\text{Sr}_3\text{CrO}_4$  compound significantly increases from 0.23 at 0 GPa to 0.37 at 30 GPa pointing towards enhanced ductility under compression shown in **Figure 7(d)**. Ductile materials have potential applications in flexible electronics as well as photovoltaic cells, as the ability to sustain mechanical deformation without fracturing is needed<sup>84</sup>. This increasing ductility with pressure is a desirable characteristic for materials used in extreme conditions where resistance to fracture is critical<sup>60</sup>. Recent studies confirm that in perovskite oxides, applied pressure can induce a shift from covalent to ionic bonding, which enhances ductility and mechanical resilience critical for applications such as solid oxide fuel cells, thermoelectric, and spintronics<sup>85,86</sup>. Agouri et al.<sup>87</sup> demonstrated through first-principles calculations on  $\text{PbXO}_3$  ( $X = \text{Ge}, \text{Si}$ ) perovskites that applied pressure induces a progressive shift from covalent to ionic bonding, thereby enhancing ductility and mechanical stability for energy applications. Similarly, Rahman et al.<sup>88</sup> reported pressure-induced transitions in  $\text{Ba}_3\text{SbI}_3$  perovskites, where bonding changes under compression were directly linked to improved ductility and optoelectronic performance.

The bulk to shear modulus ratio ( $B/G$ ) is another important indicator of ductility. A  $B/G$  ratio greater than 1.75 often correlates with ductile behavior while values less than 1.75 suggest brittleness. Both  $\text{Mg}_3\text{CrO}_4$  compounds generally maintain  $B/G$  ratios below or around 1.75 indicating brittle behavior. In contrast,  $\text{Ca}_3\text{CrO}_4$  and  $\text{Sr}_3\text{CrO}_4$  compounds  $B/G$  ratio transit from



brittle characteristics at 0-GPa and from 20GPa to 30GPa further supporting its transition to a ductile state under high pressure.

The Kleinman parameter is crucial for understanding the nature of interatomic forces with a material, specially distinguishing between bond-stretching and bond bending contributions to the elastic response. A Kleinman parameter closer to 0 indicates that bond-bending forces are more significant, while a value closer to 1 suggests a predominance of bond-stretching forces. The calculated Kleinman parameters for  $\text{Mg}_3\text{CrO}_4$ ,  $\text{Ca}_3\text{CrO}_4$ , and  $\text{Sr}_3\text{CrO}_4$  reveal a consistent decrease with increasing hydrostatic pressure (0–30 GPa). At ambient conditions, values around 0.44–0.56 indicate a balanced contribution of bond stretching and bond bending to the elastic response. However, under compression, the parameters drop toward 0.35–0.37, signifying that bond bending becomes increasingly dominant suggest a significant shift in the materials elastic behaviour: bond bending becomes increasingly dominant over bond stretching under compression<sup>89</sup>. This trend aligns with literature reports on perovskite oxides and halide crystals, where pressure enhances orbital overlap and shortens bond lengths, thereby favoring angular distortions over bond elongation. The persistence of stable Kleinman parameters across all pressures confirms the dynamical stability of these chromates, while the shift toward bond bending suggests enhanced mechanical flexibility. Such behavior is particularly relevant for piezoelectric and optoelectronic applications, where internal atomic displacements strongly influence polarization, optical absorption, and carrier transport.



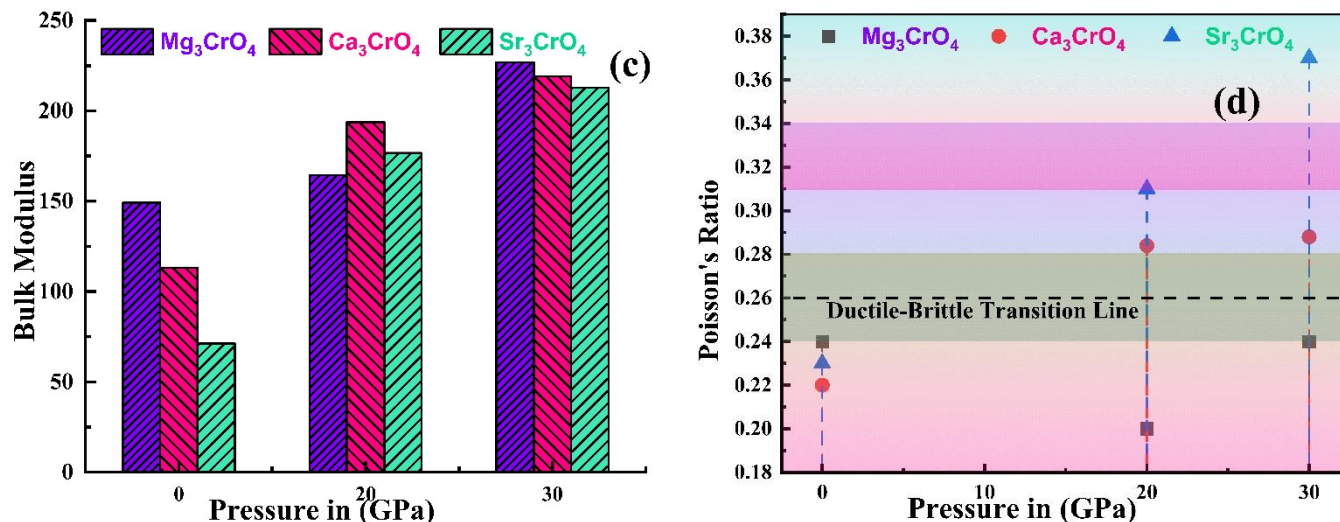


**Figure 7:** Variations of elastic constants  $C_{ij}$ , Young modulus, Bulk modulus and Poisson's ratio of  $A_3CrO_4$  compounds ( $A = Mg, Ca, Sr$ ) under hydrostatic pressures 0–30 GPa.

### 3.5 Thermal Properties and Sound Velocities

Thermodynamic stability is a fundamental requirement for materials intended for high-temperature applications, necessitating a comprehensive evaluation of their thermal behavior. Thermodynamics governs the principles of energy exchange and heat flow within physical systems, and parameters such as Debye temperature ( $\theta_D$ ) and acoustic wave velocities serve as critical indicators of thermo-physical performance. Key properties including  $\theta_D$  melting temperature ( $T_m$ ) can be derived from longitudinal ( $V_l$ ), transverse ( $V_t$ ), and average sound velocities ( $v_m$ ), in conjunction with material density ( $\rho$ ), as detailed in **Table VII**. These sound velocities were calculated using established theoretical relations and are presented in **Table VII** and illustrated in **Figure 8**.

$$v_m = \left[ \left( \frac{1}{3} \right) \left( \frac{2}{V_t^3} + \frac{1}{V_l} \right) \right]^{-\frac{1}{3}} \quad (15)$$

$$v_t = \left( \frac{G}{\rho} \right)^{\frac{1}{2}} \quad (16)$$

$$v_l = \left( \frac{B}{\rho} + \frac{4G}{3\rho} \right)^{\frac{1}{2}} \quad (17)$$



The average sound velocity is directly related to the stiffness of the materials and speed at which phonons propagate through the lattice. From **Table VII** and **Figure 8(d)** average sound velocity of  $\text{Mg}_3\text{CrO}_4$  and  $\text{Ca}_3\text{CrO}_4$  consistently increases with pressure. This trend indicates a stiffening of the crystal lattice and stronger interatomic bonds under compression which is consistent with the general increase in elastic moduli observed in such materials under pressure. Higher sound velocities typically correlate with higher Debye temperature and melting temperatures, suggesting improved thermal stability and mechanical integrity at elevated pressures. In contrast  $\text{Sr}_3\text{CrO}_4$  exhibits a more complex behavior where average sound velocity increase from 3721.06 at 0 GPa to 3898.81 at 20GPa but then slightly decrease to 3765.56 at 30GPa. This anomaly might be indicative of a pressure induced change its electronic and magnetic configurations potentially related to the magnetic reversal observed in previously analyses for  $\text{Sr}_3\text{CrO}_4$  under higher pressures.

The Debye temperature ( $\theta_D$ ) is a key parameter relates to the maximum vibration frequency of atoms in a crystal lattice, is directly linked to material stiffness and thermal conductivity. Although not directly measurable,  $\theta_D$  can be reliably estimated from elastic modulus data using the following expressions<sup>90</sup>,

$$\theta_D = \frac{h}{K_B} \left[ \frac{3n}{4\pi} \left( \frac{N_A \rho}{M} \right) \right]^{\frac{1}{3}} V_m \quad (18)$$

As presented in **Table VII** and **Figure 8(a)**, the Debye temperature generally increase with pressure indicating a stiffening of the lattice and potentially improved thermal stability. J Zhang et al.<sup>91</sup> and L Zhang et al.<sup>92</sup> reported that the Debye temperature increases with applied pressure, thereby confirming the suitability of these compounds for high-temperature applications. From **Table VII** results clearly demonstrate that the Debye temperature ( $\theta_D$ ) of  $\text{A}_3\text{CrO}_4$  compounds increases with applied pressure, consistent with previous reports. For  $\text{Mg}_3\text{CrO}_4$ ,  $\theta_D$  rises from 731.37 K at 0 GPa to 890.97 K at 30 GPa, representing a substantial increase of 159.6 K. Similarly,  $\text{Ca}_3\text{CrO}_4$  shows an increase from 621.89 K to 717.48 K, while  $\text{Sr}_3\text{CrO}_4$  increases from 445.70 K to 480.74 K over the same pressure range. This systematic enhancement of  $\theta_D$  under compression indicates stronger interatomic bonding and greater lattice rigidity, confirming the suitability of these compounds for high-temperature applications, in agreement with previous result. At 30 GPa,  $\text{Sr}_3\text{CrO}_4$  exhibits a reduction in Debye temperature, unlike  $\text{Mg}_3\text{CrO}_4$  and  $\text{Ca}_3\text{CrO}_4$ . While Mounaim



Bencheikh et al.<sup>93</sup> attributed decreases in  $\theta_D$  at constant pressure to thermal expansion and lattice softening, this mechanism is unlikely under compression where volume expansion is suppressed. The more probable origin is a pressure-induced change in the magnetic state of  $\text{Sr}_3\text{CrO}_4$  which modifies vibrational modes and reduces  $\theta_D$  highlighting the role of magneto-elastic coupling in its lattice dynamics. Among them the Mg-based compounds exhibit the highest Debye temperatures among the materials studied, indicating stronger interatomic bonding and superior phonon-mediated thermal conductivity<sup>93</sup>.

**Table VII:** GGA calculations of the Debye temperature ( $\theta_D$ , K), average sound velocity ( $v_m$ ,  $\text{m}\cdot\text{s}^{-1}$ ), Debye frequency ( $\omega_D$ , THz), melting temperature ( $T_m$ , K), and Gruneisen parameter ( $\gamma$ ) of  $\text{A}_3\text{CrO}_4$  compounds (A = Mg, Ca, Sr) under hydrostatic pressures 0–30 GPa.

	$\text{Mg}_3\text{CrO}_4$			$\text{Ca}_3\text{CrO}_4$			$\text{Sr}_3\text{CrO}_4$		
	0-GPa	20-GPa	30-GPa	0-GPa	20-GPa	30-GPa	0-GPa	20-GPa	30-GPa
<b>Debye Temperature <math>\theta_D</math></b>	731.37	831.93	890.97	621.89	691.73	717.48	445.70	489.67	480.74
<b>Average Sound Velocity</b>	5252.09	5766.36	6085.84	4875.50	5204.24	5314.84	3721.06	3898.81	3765.56
<b>Debye Frequency <math>\omega_D</math></b>	15.2	17.3	18.6	12.96	14.42	14.95	9.28	10.19	10.02
<b>Melting Temperature <math>T_m</math></b>	1965.90	2584.73	3378.80	1819.92	2868.95	3309.66	1248.19	2698.27	3177.33
<b>Gruneisen parameter</b>	1.066	1.003	1.058	1.041	1.23	1.28	1.05	1.16	1.20

The melting temperature plays a critical role in determining the thermal stability, performance, and applicability of materials across various scientific and industrial domains, including alloy design, nanoparticle stability, and high-temperature technologies<sup>94</sup>. The melting temperature ( $T_m$ ) is calculated using the following relation<sup>95</sup>.

$$T_m = 553 + 5.91C_{11} \quad (19)$$

As illustrated in **Table VII** and **Figure 8(c)**, the melting temperature  $T_m$  is consistently predicted to increase significantly with pressure for all chromates. The calculated melting temperatures ( $T_m$ ) of  $\text{A}_3\text{CrO}_4$  compounds show a clear increasing trend with pressure, reflecting enhanced lattice stability under compression. For  $\text{Mg}_3\text{CrO}_4$ ,  $T_m$  rises from 1965.90 K at 0 GPa to 3378.80 K at 30 GPa.  $\text{Ca}_3\text{CrO}_4$  exhibits a similar increase, from 1819.92 K to 3309.66 K, while  $\text{Sr}_3\text{CrO}_4$  shows the most pronounced change, from 1248.19 K to 3177.33 K over the same pressure range. These results indicate that hydrostatic compression significantly strengthens interatomic bonding, thereby elevating the melting point<sup>96</sup>. The systematic increase in  $T_m$  confirms the suitability of



these compounds for high-temperature applications, consistent with literature reports that pressure enhances thermal stability in oxide materials<sup>97</sup>. This strong correlation between pressure and melting temperature suggests that these materials can withstand much higher temperatures at elevated pressures which is a critical consideration for high temperature and high-pressure applications. Such high melting points are characteristics of robust ceramic materials<sup>60</sup>.

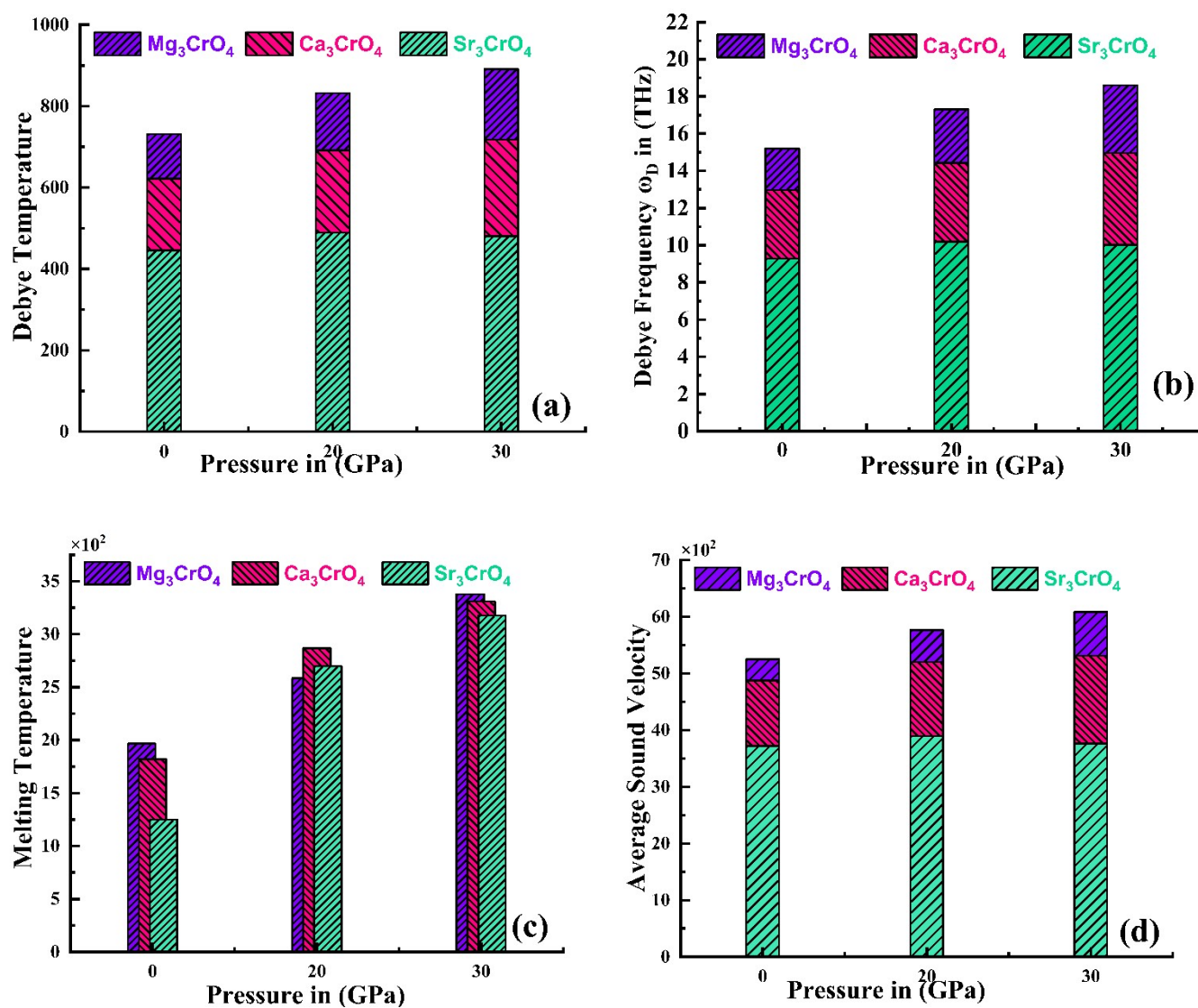


**Figure 8:** Variations of Debye Temperature, Average sound velocity, Debye frequency, melting temperature of  $A_3CrO_4$  compounds ( $A = Mg, Ca, Sr$ ) under hydrostatic pressures 0–30 GPa.



The Debye frequency ( $\omega_D$ ) is a measure of the maximum vibrational frequency of atoms in a crystal lattice serving as a fundamental parameter in solid-state physics for understanding thermal properties. The Debye frequency for a given solid is calculated using the following expression<sup>94</sup>.

$$\omega_D = K_B \cdot \frac{\theta_D}{h} \quad (19)$$

From **Table VII** and **Figure 8(b)**,  $Mg_3CrO_4$  the Debye frequency increases from 15.2 THz at 0 GPa to 18.6 THz at 30 GPa. Similarly,  $Ca_3CrO_4$  Debye frequency also shows an increase from 12.96 THz to 14.95 THz. This increase signifies an enhanced stiffness of the phonon nodes under pressure implying a stronger lattice that can sustain higher frequency vibrations. For  $Sr_3CrO_4$  the Debye frequency increase from 9.28 THz at 0 GPa to 10.19 THz at 20 GPa but then slightly decrease to 10.02 THz at 30 GPa, mirroring the trend observed in its average sound velocity. This behavior reinforces the hypothesis of a pressure induced events affecting the lattice dynamics of  $Sr_3CrO_4$ <sup>98</sup>. Materials with higher Debye frequencies are generally expected to have higher thermal conductivities and specific heats making these chromates potentially suitable for applications requiring efficient heat dissipation of thermal insulation under specific conditions.

**Table VII** also report the Gruneisen parameter ( $\gamma$ ), which quantifies anharmonicity of the lattice vibrations and the relationship between thermal expansion and changes in vibrational frequencies with volume. It is a parameter for understanding a materials thermal expansion coefficient and its response to temperature changes under pressure. This parameter is derived from Poisson's ratio using the following relation<sup>99</sup>.

$$\gamma = \frac{3(1 + \nu)}{2(2 - 3\nu)} \quad (20)$$

The calculated values for investigated compounds under pressure remain close to unity, indicating moderate anharmonicity. A positive Gruneisen parameter implies that phonon frequencies increase upon compression, which is typical for most solids. The variations in this parameter provide insights into how each material's thermal properties will respond to external pressure, influencing applications where thermal stability and dimensional changes are critical. The observed increase in  $\gamma$  with pressure for  $Ca_3CrO_4$  and  $Sr_3CrO_4$  is consistent with literature reports Mounaim Bencheikh et al.<sup>93</sup> that compression amplifies anharmonic lattice responses by modifying phonon frequencies. In contrast,  $Mg_3CrO_4$  shows only weak variation, suggesting



greater anharmonic stability under hydrostatic compression. Overall, the results confirm that pressure enhances anharmonic effects in  $A_3CrO_4$  compounds, while the magnitude of  $\gamma$  remains within the range typical for stable oxide materials. For instance, materials with low Gruneisen parameters tend to have low thermal expansion coefficients, desirable for precision components operating over wide temperature ranges<sup>100</sup>.

The observed pressure induced magnetic transition in our investigated compounds in the magnetic data discussed previously alongside the elastic property changes further emphasizes the intricate interplay between structural, electronic, elastic, thermodynamics and magnetic degrees of freedom in these materials.

In conclusion, the variations in average sound velocity, Debye frequency, and Gruneisen parameter with pressure provide a comprehensive picture of the lattice dynamics and thermal behavior of  $Mg_3CrO_4$ ,  $Ca_3CrO_4$  and  $Sr_3CrO_4$ . The consistent stiffening and enhanced thermal stability observed in  $Mg_3CrO_4$  and  $Ca_3CrO_4$  make them promising for high-pressure and high-temperature applications. The anomalous behavior of  $Sr_3CrO_4$ , particularly the decrease in sound velocity and Debye frequency at higher pressures, suggests a pressure-induced phenomenon that indicate further investigation, potentially leading to new applications in pressure-tunable functional materials. These findings contribute to the broader understanding of complex oxides and their potential in advancing materials science and engineering.

### 3. Conclusion

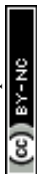
This study delivers a comprehensive DFT-based exploration of  $A_3CrO_4$  ( $A = Mg, Ca, Sr$ ) chromates under hydrostatic pressures up to 30 GPa, employing GGA-PBE, GGA-PBEsol, and GGA+U functionals to capture their structural, electronic, magnetic, elastic, and thermal responses.  $Mg_3CrO_4$  and  $Ca_3CrO_4$  consistently retain ferromagnetic half-metallicity, exhibit lattice stiffening, rising Debye temperatures and frequencies, and increasing melting points, confirming their robustness for high-temperature and high-pressure applications.  $Sr_3CrO_4$ , in contrast, shows anomalous pressure-dependent behavior, including magnetic moment reversal and reductions in sound velocity and Debye frequency at higher pressures, pointing to a unique pressure-induced phase transition. Elastic constant analysis verifies dynamic stability across all compounds, with ductility transitions observed in  $Ca_3CrO_4$  and  $Sr_3CrO_4$  under compression. Electronic structure



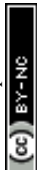
calculations further reveal persistent half-metallicity across all compounds, with spin-down channels maintaining wide band gaps and spin-up channels displaying metallic behavior. The inclusion of Hubbard corrections (GGA+U) strengthens the reliability of these electronic predictions, confirming the robustness of the band structure and magnetic ordering. Collectively, these results establish  $\text{Mg}_3\text{CrO}_4$  and  $\text{Ca}_3\text{CrO}_4$  as promising candidates for spin-injection layers and ceramic applications, while  $\text{Sr}_3\text{CrO}_4$  emerges as a potential pressure-tunable functional material. Overall, the findings advance the understanding of complex oxides and highlight their potential in next-generation spintronic and high-performance technologies.

## Reference

1. Gish, J. T., Lebedev, D., Song, T. W., Sangwan, V. K. & Hersam, M. C. Van der Waals opto-spintronics. *Nature Electronics* 2024 7:5 7, 336–347 (2024).
2. Niu, Y., Wang, Y., Wang, L., Sun, Y. & Wang, P. Unveiling the spin polarization mechanism in half-metallic  $\text{CrO}_2$  regulated by crystal plane orientation. *New Journal of Chemistry* 49, 17802–17807 (2025).
3. Sierra, J. F., Fabian, J., Kawakami, R. K., Roche, S. & Valenzuela, S. O. Van der Waals heterostructures for spintronics and opto-spintronics. *Nature Nanotechnology* 2021 16:8 16, 856–868 (2021).
4. Chaudhary, V. *et al.* Spin and current transport in the robust half-metallic magnet  $\text{c-CoFeGe}$ . *Journal of Physics: Condensed Matter* 35, 285502 (2023).
5. Peng, K. *et al.* A DFT study on half-metallicity of Ruddlesden–Popper layered perovskite  $\text{Bi}_8\text{Ba}_4\text{Mn}_8\text{O}_{28}$ . *Physica B Condens. Matter* 674, 415587 (2024).
6. Oguz, I. C., Jaouen, F. & Mineva, T. Exploring Spin Distribution and Electronic Properties in  $\text{FeN}_4$ -Graphene Catalysts with Edge Terminations. *Molecules* 2024, Vol. 29, 29, (2024).
7. Wei, X. P., Mei, Z. Y. & Tao, X. Surface effects for half-metallic Heusler alloy  $\text{CrYCoAl}$ . *Physica B Condens. Matter* 683, 415925 (2024).
8. Zou, Y. *et al.* First-Principles Study on Mechanical, Electronic, and Magnetic Properties of Room Temperature Ferromagnetic Half-Metal  $\text{MnNCl}$  Monolayer. *Nanomaterials* 2023, Vol. 13, 13, (2023).
9. Hu, X. Half-metallic antiferromagnet as a prospective material for spintronics. *Advanced Materials* 24, 294–298 (2012).
10. Mavropoulos, P., Ležaić, M. & Blügel, S. Half-metallic ferromagnets for magnetic tunnel junctions by *ab initio* calculations. *Phys. Rev. B* 72, 174428 (2005).



11. Shaughnessy, M., Snow, R., Damewood, L. & Fong, C. Y. Memory and Spin Injection Devices Involving Half Metals. *J. Nanomater.* **2011**, 140805 (2011).
12. Yakout, S. M. Spintronics: Future Technology for New Data Storage and Communication Devices. *Journal of Superconductivity and Novel Magnetism* **2020** *33:9* **33**, 2557–2580 (2020).
13. Parkin, S. S. P. *et al.* Exchange-biased magnetic tunnel junctions and application to nonvolatile magnetic random access memory (invited). *J. Appl. Phys.* **85**, 5828–5833 (1999).
14. De Groot, R. A., Mueller, F. M., Engen, P. G. V. & Buschow, K. H. J. New Class of Materials: Half-Metallic Ferromagnets. *Phys. Rev. Lett.* **50**, 2024 (1983).
15. Fakhim Lamrani, A. *et al.* Half metallic antiferromagnetic behavior in doped TiO<sub>2</sub> rutile with double impurities (Os, Mo) from ab initio calculations. *Thin Solid Films* **570**, 45–48 (2014).
16. Cerón, J. A. G., Téllez, D. A. L. & Roa-Rojas, J. Weak Ferromagnetism in the FeCr<sub>2</sub>O<sub>4</sub> Semiconductor Spinel with Half-Metallic Feature in the Ground State. *Journal of Electronic Materials* **2021** *51:2* **51**, 822–830 (2021).
17. Feng, L., Wang, F., Li, J. & Wang, S. J. A First-Principles Study of Half-Metallic Full-Heusler Compound Ti<sub>2</sub>CoSi. *Applied Mechanics and Materials* **320**, 394–398 (2013).
18. Chen, W. T. *et al.* A half-metallic A- and B-site-ordered quadruple perovskite oxide CaCu<sub>3</sub>Fe<sub>2</sub>Re<sub>2</sub>O<sub>12</sub> with large magnetization and a high transition temperature. *Nature Communications* **2014** *5:1* **5**, 1–7 (2014).
19. Yi, K., Tang, Q., Wu, Z., Gu, J. & Zhu, X. Structural, magnetic, and electrical transport properties of half-metallic double perovskite La<sub>2</sub>CrNiO<sub>6</sub> oxides. *J. Alloys Compd.* **933**, 167742 (2023).
20. Dar, S. A., Srivastava, V. & Sakalle, U. K. Structural, elastic, mechanical, electronic, magnetic, thermoelectric and thermodynamic investigation of half metallic double perovskite oxide Sr<sub>2</sub>MnTaO<sub>6</sub>. *J. Magn. Magn. Mater.* **484**, 298–306 (2019).
21. Kumar, A., Kumar, M. & Singh, R. P. Magnetic, opto-electronic, and thermodynamic properties of half-metallic double perovskite oxide, Ba<sub>2</sub>YbTaO<sub>6</sub>: a density functional theory study. *Journal of Materials Science: Materials in Electronics* **2021** *32:10* **32**, 12951–12965 (2021).
22. Chen, Y. *et al.* Density Functional Theory Study of Nonvolatile Electrical Control of Half-Metallicity in Multiferroic RuCl<sub>2</sub>/Al<sub>2</sub>S<sub>3</sub> Heterostructures: Implications for Spin Memory Devices. *ACS Appl. Nano Mater.* **7**, 4302–4312 (2024).
23. Jin, C. *et al.* Ferroelectric modulated giant valley polarization and half metallicity in 2D RuBrF/Sc<sub>2</sub>CO<sub>2</sub> multiferroic heterostructure for non-volatile memory applications. *J. Appl. Phys.* **138**, (2025).



24. Hameed, U. *et al.* First-principles calculations to investigate magnetic, electronic, and thermoelectric response of europium-based half metallic ternary Zintl compounds  $\text{EuMg}_2\text{X}_2$  (X=Sb and Bi). *Journal of Physics and Chemistry of Solids* **199**, 112519 (2025).
25. Zada, Z. *et al.* Structure stability, half metallic ferromagnetism, magneto-electronic and thermoelectric properties of new zintl  $\text{XCr}_2\text{Bi}_2$  (X=Ca, Sr) compounds for spintronic and renewable energy applications. *Physica B Condens. Matter* **607**, 412866 (2021).
26. Balke, B. *et al.* Doped semiconductors as half-metallic materials: Experiments and first-principles calculations of  $\text{Co Ti}_{1-x}\text{M}_x\text{Sb}$  (M=Sc, V, Cr, Mn, Fe). *Phys. Rev. B Condens. Matter Mater. Phys.* **77**, 045209–045209 (2008).
27. Seong, S. *et al.* Experimental evidence for mixed-valent Cr ions in half-metallic  $\text{CrO}_2$ : Temperature-dependent XMCD study. *J. Magn. Magn. Mater.* **452**, 447–450 (2018).
28. Barouni, S. *et al.* First-principles prediction of half metallic-ferromagnetism in  $\text{La}_{0.25}\text{Sr}_{0.75}\text{Sn}_{0.4}\text{In}_{0.25}\text{Ru}_{0.35}\text{O}_3$  and enhanced experimental electrical and magnetic behaviours. *Physical Chemistry Chemical Physics* **26**, 18102–18112 (2024).
29. Parray, R. A. & Ravichandran, K. Experimental studies of  $\text{Cr}_2\text{NiAl}$  half-metallic inverse Heusler compound for spintronic applications. *Journal of Materials Science: Materials in Electronics* **2023 34:7 34**, 1–10 (2023).
30. Ramdane, O., Labidi, M., Labidi, S. & Masrour, R. A comparative study on the structural, electronic, and magnetic properties of the cubic Sr-based perovskite  $\text{SrXO}_3$  (X = Mn, Sn, Cr): DFT calculation. *Journal of the Korean Ceramic Society* **2024 61:6 61**, 993–1005 (2024).
31. Jamil, M. *et al.* A DFT theoretical prediction of new half-metallic ferromagnetism, mechanical stability, optoelectronic and thermoelectric properties of  $\text{ZnCrO}_3$  perovskites for spintronic applications. *Solid State Commun.* **394**, 115702 (2024).
32. Erum, N. *et al.* First-principles studies on physical properties for new half-metallic perovskites  $\text{AFeO}_3$  (A = Ca, Sr, Ba): Spintronics and energy harvesting applications. *Int. J. Quantum Chem.* **124**, e27363 (2024).
33. Prateek, K. *et al.* Magnetotransport properties of  $\text{CrO}_2$  nanowires fabricated by selective area growth. *Journal of Physics and Chemistry of Solids* **178**, 111350 (2023).
34. Aly, A. E. & Rai, D. P. A DFT Study of Electronic and Magnetic Properties of  $\text{Cr}_2\text{O}_3$  using Spin-Polarized Approach. *International Journal of Computational Physics Series* **1**, 91–96.
35. Rimmler, B. H., Pal, B. & Parkin, S. S. P. Non-collinear antiferromagnetic spintronics. *Nat. Rev. Mater.* **10**, 109–127 (2025).
36. Monir, M. E. A. *et al.* Structural, elastic, electronic, magnetic and thermal properties of  $\text{X}_3\text{FeO}_4$  (X = mg, ca and Sr) materials. *Scientific Reports* **2025 15:1 15**, 2957- (2025).



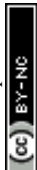
37. Perdew, J. P. & Zunger, A. Self-interaction correction to density-functional approximations for many-electron systems. *Phys. Rev. B* **23**, 5048 (1981).
38. Ceperley, D. M. & Alder, B. J. Ground State of the Electron Gas by a Stochastic Method. *Phys. Rev. Lett.* **45**, 566 (1980).
39. Segall, M. D. *et al.* First-principles simulation: ideas, illustrations and the CASTEPcode. *Journal of Physics: Condensed Matter* **14**, 2717 (2002).
40. Pfrommer, B. G., Côté, M., Louie, S. G. & Cohen, M. L. Relaxation of Crystals with the Quasi-Newton Method. *J. Comput. Phys.* **131**, 233–240 (1997).
41. Banik, B., Shamima Khanom, M., Hossain, M. R. & Ahmed, F. Computational evaluation of pressure effects on cubic ferromagnetic perovskites  $\text{ACrBr}_3$  ( $A = \text{K, Rb, Cs, Fr}$ ): materials engineering perspectives for spintronics and optoelectronics via DFT. *Mater. Adv.* <https://doi.org/10.1039/D6MA00182C> (2026) doi:10.1039/D6MA00182C.
42. Payne, M. C., Teter, M. P., Allan, D. C., Arias, T. A. & Joannopoulos, J. D. Iterative minimization techniques for *ab initio* total-energy calculations: molecular dynamics and conjugate gradients. *Rev. Mod. Phys.* **64**, 1045 (1992).
43. Vensky, S. *et al.* The real structure of  $\text{Na}_3\text{BiO}_4$  by electron microscopy, HR-XRD and PDF analysis. *Zeitschrift fur Kristallographie* **220**, 231–244 (2005).
44. Boulekbache, M. E. A. *et al.* Structural, magnetic, electronic, and thermodynamic properties of  $\text{Ba}_2\text{ScMO}_6$  ( $M = \text{Ru, Os}$ ) double perovskites. *Journal of Materials Science* **2026** 1–14 (2026) doi:10.1007/S10853-026-12725-9.
45. Belhachi, S. *et al.* DFT Analysis of  $\text{Ba}_2\text{NbRhO}_6$ : A Promising Double Perovskite for Sustainable Energy Applications. *J. Inorg. Organomet. Polym. Mater.* **35**, 978–993 (1234).
46. Monir, M. E. A. *et al.* Structural, elastic, electronic, magnetic and thermal properties of  $\text{X}_3\text{FeO}_4$  ( $X = \text{mg, ca and Sr}$ ) materials. *Scientific Reports* **2025** 15:1 **15**, 2957- (2025).
47. Sofi, M. Y., Khan, M. S. & Khan, M. A. Materials Advances candidates for semiconductor spintronics and. 4913–4931 (2024) doi:10.1039/d3ma01160g.
48. Nazir, S. *et al.* Investigation of Opto-Electronic and Thermoelectric Characteristics of Halide Perovskite  $\text{CdLiCl}_3$  for Energy Conversion Applications at Different Pressure. *Journal of Inorganic and Organometallic Polymers and Materials* **2024** 35:1 **35**, 493–502 (2024).
49. Ahmad Khandy, S. & Gupta, D. C. DFT analogue of prospecting the spin-polarised properties of layered perovskites  $\text{Ba}_2\text{ErNbO}_6$  and  $\text{Ba}_2\text{TmNbO}_6$  influenced by electronic structure. *Scientific Reports* | **12**, 19690 (123AD).
50. Gautam, S., Ghosh, S., Dinesh, & Gupta, C. Understanding the computational insights of spin-polarised density functional theory into the newly half-metallic f electron-based actinide perovskites  $\text{SrMO}_3$  ( $M = \text{Pa, Np, Cm, Bk}$ ). *Scientific Reports* | **13**, 16882 (123AD).



51. Firdous, F. *et al.* Half-metallicity, magnetic and optical attributes of mechanically stable half-Heusler VSnX (X = Pt, Pd) alloys for spintronics: a DFT study. *The European Physical Journal Plus* 2023 138:8 **138**, 699- (2023).
52. Ahmad, M. *et al.* Intrinsic Room-Temperature Ferromagnetism in New Halide Perovskite AgCrX<sub>3</sub> (X: F, Cl, Br, I) Using Ab Initio and Monte Carlo Simulations. *ACS Omega* **9**, 18148–18159 (2024).
53. Islam, R. & Borah, J. P. Electronic structure and magnetic properties investigation of cubic Fe<sub>3</sub>O<sub>4</sub>. *Mater. Today Proc.* **68**, 159–162 (2022).
54. Chang, J. *et al.* On the electronic structure and magnetism of CaCrO<sub>3</sub>: A hybrid-exchange density-functional-theory study. *Mater. Today Commun.* **27**, 102179 (2021).
55. Ullah, H. *et al.* Mechanical and magneto-electronic properties of europium lanthanide-based cubic perovskites EuYO<sub>3</sub> (Y=Cr, Mn, Fe): An ab initio study. *Journal of Rare Earths* **42**, 562–569 (2024).
56. Kabi, O. *et al.* Ab Initio Investigation of the Structural, Elastic, Dynamic, Electronic, and Magnetic Properties of Cubic Perovskite CeCrO<sub>3</sub>. *ACS Omega* **9**, 11820–11828 (2024).
57. Agouri, M. *et al.* First-principles calculations to investigate structural, electronic, elastic and thermodynamic properties of PbXO<sub>3</sub> (X = Ge, Si) perovskites under pressure effect for energy applications. *Chemical Papers* 2025 80:2 **80**, 1387–1398 (2025).
58. Nazir, S., Algethami, A. A. & Musa Saad, M. Evolution of metallicity, enhancement of TC and magnetic anisotropy energy in Y<sub>2</sub>NiIrO<sub>6</sub>: Hydrostatic ([111]) strain influence. *Journal of Physics and Chemistry of Solids* **197**, 112410 (2025).
59. Shi, J., Fernando, G. W., Dang, Y., Suib, S. L. & Jain, M. Structural and electronic properties of rare-earth chromites: A computational and experimental study. *Phys. Rev. B* **106**, 165117 (2022).
60. Ullah, H. *et al.* Mechanical and magneto-electronic properties of europium lanthanide-based cubic perovskites EuYO<sub>3</sub> (Y=Cr, Mn, Fe): An ab initio study. *Journal of Rare Earths* **42**, 562–569 (2024).
61. Bouldiab, Y. *et al.* Strong half-metallic ferromagnetism and thermoelectric response in new half-Heusler RbCrX (X = Sb, As) alloys: first-principles calculations. *Indian Journal of Physics* 2021 96:10 **96**, 2755–2778 (2021).
62. Nor, N. A. N. M. *et al.* Influence of Hubbard U correction on the structural, electronic and optical properties of Kesterite Cu<sub>2</sub>XSnS<sub>4</sub> (X= Zn, Fe). *Physica B Condens. Matter* **673**, 415450 (2024).
63. Shen, G. *et al.* The first principle research of CaO and MgO particulate heterogeneous nucleation in Mg alloys. *Appl. Surf. Sci.* **593**, 153224 (2022).



64. Ramdane, O., Labidi, M., Labidi, S. & Masrour, R. A comparative study on the structural, electronic, and magnetic properties of the cubic Sr-based perovskite SrXO<sub>3</sub> (X = Mn, Sn, Cr): DFT calculation. *Journal of the Korean Ceramic Society* 2024 61:6 **61**, 993–1005 (2024).
65. El-harrar, Y. *et al.* Study of optoelectronics and magnetic properties of GdCrWO<sub>6</sub> oxide by ab initio calculations. *Computational Condensed Matter* **38**, e00859 (2024).
66. Tiwari, S. & Mishra, A. Effect of Ionic Radii Variation on the Structural, Electrical, Dielectric, and Magnetic Characteristics of Orthochromite RCrO<sub>3</sub> (R = La, Y, Gd). *Journal of Superconductivity and Novel Magnetism* 2024 37:3 **37**, 623–637 (2024).
67. Su, W. *et al.* Structure and magnetic properties of electrospun rare earth orthochromites nanofibers. *Solid State Sci.* **145**, 107314 (2023).
68. Schechter, M., Syljuåsen, O. F. & Paaske, J. Nematic Bond Theory of Heisenberg Helimagnets. *Phys. Rev. Lett.* **119**, 157202 (2017).
69. Yang, L. *et al.* Absence of spin transport in amorphous YIG evidenced by nonlocal spin transport experiments. *Phys. Rev. B* **104**, 144415 (2021).
70. Jabar, A., Benyoussef, S. & Bahmad, L. Study of Physical Characteristics of the New Half-Heusler Alloy BaHgSn by DFT Analysis. <https://arxiv.org/pdf/2403.08483> (2024).
71. De Groot, R. A., Mueller, F. M., Engen, P. G. V. & Buschow, K. H. J. New Class of Materials: Half-Metallic Ferromagnets. *Phys. Rev. Lett.* **50**, 2024 (1983).
72. Pingak, R. K. *et al.* Structural, Electronic, Elastic, and Optical Properties of Cubic BaLiX<sub>3</sub> (X = F, Cl, Br, or I) Perovskites: An Ab-initio DFT Study. *Indonesian Journal of Chemistry* **23**, 843–862 (2023).
73. Wu, Z. J. *et al.* Crystal structures and elastic properties of superhard Ir N<sub>2</sub> and Ir N<sub>3</sub> from first principles. *Phys. Rev. B Condens. Matter Mater. Phys.* **76**, 054115 (2007).
74. Goumri-Said, S. & Kanoun, M. B. Theoretical investigations of structural, elastic, electronic and thermal properties of Damiaoite PtIn<sub>2</sub>. *Comput. Mater. Sci.* **43**, 243–250 (2008).
75. Gao, J., Liu, Q. J. & Tang, B. Elastic stability criteria of seven crystal systems and their application under pressure: Taking carbon as an example. *J. Appl. Phys.* **133**, (2023).
76. Mehl, M. J. Pressure dependence of the elastic moduli in aluminum-rich Al-Li compounds. *Phys. Rev. B* **47**, 2493 (1993).
77. Sun, Z., Li, S., Ahuja, R. & Schneider, J. M. Calculated elastic properties of M<sub>2</sub>AlC (M=Ti, V, Cr, Nb and Ta). *Solid State Commun.* **129**, 589–592 (2004).
78. Jasiukiewicz, C. & Karpus, V. Debye temperature of cubic crystals. *Solid State Commun.* **128**, 167–169 (2003).



79. Wachter, P., Filzmoser, M. & Rebizant, J. Electronic and elastic properties of the light actinide tellurides. *Physica B Condens. Matter* **293**, 199–223 (2001).
80. Mehl, M. J., Osburn, J. E., Papaconstantopoulos, D. A. & Klein, B. M. Structural properties of ordered high-melting-temperature intermetallic alloys from first-principles total-energy calculations. *Phys. Rev. B* **41**, 10311 (1990).
81. Shen, G. *et al.* The first principle research of CaO and MgO particulate heterogeneous nucleation in Mg alloys. *Appl. Surf. Sci.* **593**, 153224 (2022).
82. Ali, M. A. *et al.* Modeling of structural, elastic, mechanical, acoustical, electronic and thermodynamic properties of XPdF<sub>3</sub> (X = Rb, Tl) perovskites through density functional theory. *Phys. Scr.* **95**, (2020).
83. Kabi, O. *et al.* Ab Initio Investigation of the Structural, Elastic, Dynamic, Electronic, and Magnetic Properties of Cubic Perovskite CeCrO<sub>3</sub>. *ACS Omega* **9**, 11820–11828 (2024).
84. Banik, B., Shamima Khanom, M., Hossain, M. R. & Ahmed, F. Computational evaluation of pressure effects on cubic ferromagnetic perovskites ACrBr<sub>3</sub> (A = K, Rb, Cs, Fr): materials engineering perspectives for spintronics and optoelectronics via DFT. *Mater. Adv.* <https://doi.org/10.1039/D6MA00182C> (2026) doi:10.1039/D6MA00182C.
85. Li, X. *et al.* High pressure and Ti promote oxygen vacancies in perovskites for enhanced thermoelectric performance. *J. Alloys Compd.* **922**, 166247 (2022).
86. Hilpert, K. *et al.* Defect formation and mechanical stability of perovskites based on LaCrO<sub>3</sub> for solid oxide fuel cells (SOFC). *J. Eur. Ceram. Soc.* **23**, 3009–3020 (2003).
87. Agouri, M. *et al.* First-principles calculations to investigate structural, electronic, elastic and thermodynamic properties of PbXO<sub>3</sub> (X = Ge, Si) perovskites under pressure effect for energy applications. *Chemical Papers 2025 80:2* **80**, 1387–1398 (2025).
88. Rahman, M. F. *et al.* A novel investigation of pressure-induced semiconducting to metallic transition of lead free novel Ba<sub>3</sub>SbI<sub>3</sub> perovskite with exceptional optoelectronic properties. *RSC Adv.* **14**, 11169–11184 (2024).
89. Alathlawi, H. J. *et al.* Pressure-Induced Effects on BaPbO<sub>3</sub>: A Prospectively Valuable Material for Piezoelectric Applications via DFT. *Crystal Research and Technology* **59**, 2300293 (2024).
90. Anderson, O. L. A simplified method for calculating the debye temperature from elastic constants. *Journal of Physics and Chemistry of Solids* **24**, 909–917 (1963).
91. Zhang, J. *et al.* Electronic structure, mechanical, optical and thermodynamic properties of cubic perovskite InBeF<sub>3</sub> with pressure effects: First-principles calculations. *Results Phys.* **50**, 106590 (2023).



92. Zhang, L. *et al.* Structural stability, mechanical, and thermodynamic properties under pressure of B2-type CuM (M = Be, Al, and Zn) alloys: a DFT investigation. *Phys. Scr.* **99**, 065946 (2024).
93. Bencheikh, M. & El Farh, L. First-principles study of the thermodynamic properties of the bulk cubic compound InTe at high temperature and pressure. *Next Materials* **9**, 101254 (2025).
94. Tarekuzzaman, M. *et al.* DFT analysis of structural, electronic, optical, and thermodynamic properties of LiXI<sub>3</sub> (where X = Ca, Sr, Ba) halide perovskites for optoelectronics. *Sci. Rep.* **15**, 1–23 (2025).
95. Fine, M. E., Brown, L. D. & Marcus, H. L. Elastic constants versus melting temperature in metals. *Scripta Metallurgica* **18**, 951–956 (1984).
96. Tahsin Özer & Nihat Arıkan. The Implications of Pressure on Mechanical and Thermodynamic Properties of Ni<sub>2</sub>X (X = Sc, Ti, V)Al: DFT Calculation. *Russian Journal of Physical Chemistry A* 2024 98:4 **98**, 669–682 (2024).
97. Dar, S. A., Srivastava, V. & Sakalle, U. K. Ab Initio High Pressure and Temperature Investigation on Cubic PbMoO<sub>3</sub> Perovskite. *Journal of Electronic Materials* 2017 46:12 **46**, 6870–6877 (2017).
98. Jebari, H. *et al.* First-principles calculations to investigate structural, electronic, optical, thermoelectric, magnetic, and magnetocaloric properties of the orthochromite EuCrO<sub>3</sub>. *Comput. Theor. Chem.* **1220**, 113993 (2023).
99. Clarke, D. R. Materials selections guidelines for low thermal conductivity thermal barrier coatings. *Surf. Coat. Technol.* **163–164**, 67–74 (2003).
100. Satapathy, S., Batouche, M., Seddik, T., Salah, M. M. & Maurya, K. K. First Principle Study on Structural, Thermoelectric, and Magnetic Properties of Cubic CdCrO<sub>3</sub> Perovskites: A Comprehensive Analysis. *Crystals* 2023, Vol. 13, **13**, (2023).

